Final Report Draft

<u>Project 22-019</u>

Refining ammonia emissions using inverse modeling and satellite observations over Texas and the Gulf of Mexico and investigating its effect on fine particulate matter

Prepared for

Texas Air Quality Research Program

(AQRP)

PREPARED BY

University of Houston

4800 Calhoun Road

Houston, Texas 77204-5007

Principal Investigator

Yunsoo Choi

August, 2023

5

Executive Summary

Ammonia (NH_3) can be harmful by affecting air quality and human health due to its contributions to inorganic particulate matter and climate change. The limited observations of NH_3 lead to uncertainty in its emission estimates, thereby hindering effective management and control of its adverse impacts. In this project, the UH AQF team updated NH_3 emissions using an inverse modeling study over Texas and the Gulf of Mexico. The Community Multiscale Air Quality (CMAQ) model was employed, integrating NH_3 remote sensing data from the Cross-track Infrared Sounder (CrIS) and the Infrared Atmospheric Sounding Interferometer (IASI) for 2019. A data gap, spanning from March 25 to August 12 in 2019 due to unavailable CrIS observations, complicated the exclusive use of CrIS satellite data for annual NH_3 emissions adjustments. To compensate for this, IASI observational data was incorporated. The National Emissions Inventory (NEI) 2017 was employed to generate NH_3 emissions from mobile, area, and point sources, encompassing both anthropogenic and biogenic sources. The inverse modeling study utilized the iterative Finite Difference Mass Balance (iFDMB) technique to refine NH_3 emissions based on CrIS and IASI data. To streamline computation and ensure prediction accuracy, a reduced complexity CMAQ model (RCCM) was implemented for simulations. Utilizing the revised emissions, an assessment was carried out to determine the impact on NEI emissions over Texas and the Gulf of Mexico when constrained by satellite data. This study offered valuable insights into the advantages of integrating satellite data into emission estimations.

By using satellite data to improve emissions inventory over Texas, project 22-019 directly addressed the priority research areas set by the Air Quality Research Program (AQRP). The project's primary objectives were:

1. Improving NH_3 emissions using the iFDMB inverse modeling technique, incorporating both the developed reduced complexity model and satellite data.
2. Investigating the effect of updated NH_3 emissions on inorganic fine particulate matter ($PM_{2.5}$) concentrations.

Both objectives were accomplished, as summarized below:

The reduced complexity model was successfully developed. Comparing its results with the standard CMAQ model displayed its accuracy while also lessening the computational load. Using

the iFDMB method formulated by Momeni et al. (2023), NH_3 emissions were updated for 2019 using CrIS and IASI data. In general, results showed an increase in NH_3 emissions compared to prior emissions, which occurred due to higher NH_3 levels observed by satellites. Annual emissions surged by over 100 tons in Northwestern Texas and by over 50 tons in Southeastern areas. In regions where prior emissions were nonexistent or negligible in Texas, the emissions augmented between 10 and 50 tons. The Gulf of Mexico also saw significant growth, with emissions rising from zero to more than 50 tons. Across Texas, NH_3 concentrations have shown an increase, with the most pronounced surge seen in Northwestern areas, where levels climbed between 3-4 ppb. In the rest of Texas, the escalation ranged between 1-2 ppb. Over the Gulf of Mexico, a 1-2 ppb increase in NH_3 concentrations underscores the influential role of maritime and oil industry activities.

As for the influence of updated ammonia emissions on inorganic $PM_{2.5}$, ammonium (NH_4^+) concentrations across Texas rose marginally, with a more marked increase in the state's eastern parts. Over the Gulf of Mexico, NH_4^+ levels saw a more pronounced spike than in Texas. Concerning sulfate (SO_4^{2-}) concentrations, there was a more significant increase in Eastern Texas, particularly in areas with already high a-prior SO_4^{2-} levels. The significant increase in SO_4^{2-} concentrations near the Port Arthur and Galveston regions highlights the potential impact of human activities like industrial operations and shipping. Regarding nitrate (NO_3^-), there were increases across Texas, indicating that the elevated NH_3 possibly fostered an ammonia-rich environment that facilitates the neutralization of SO_4^- to promote NO_3^- production. The enhanced a-posteriori NO_3^- concentrations along the shoreline in the Gulf of Mexico are also of note.

Future recommendations:

- Implementing advanced data assimilation methods, like the 4-Dimensional variational approach, to refine ammonia emissions.
- Employing a combination of IASI and CrIS satellite data for more accurate refinement of ammonia emissions.
- Calibrating CrIS and IASI data over Texas to ensure precise measurements.

- Using advanced sensitivity analysis techniques (such as the decoupled direct method, adjoint) to accurately specify the contribution of each sector to ammonia concentrations and inorganic fine particulate matter.
- Conducting multi-year studies to update ammonia emissions, helping to address issues related to year-to-year variations, particularly over the Gulf of Mexico.
- Examining the specific source-contributions to the elevated ammonia levels detected in the Port Arthur and Galveston area, as well as in southeast Texas.

1. Introduction

This document provides the final report for the Texas Air Quality Research Program (AQRP) Project 22-019, "Refining ammonia emissions using inverse modeling and satellite observations over Texas and the Gulf of Mexico and investigating its effect on the fine particulate matter". The goal of Project 22-019 is to update NH_3 emissions over the Texas and Gulf of Mexico. The project Principal Investigator is Dr. Yunsoo Choi (University of Houston). The AQRP project manager is Dr. Elena McDonald-Buller at the University of Texas, Austin. The project liaison for the Texas Commission on Environmental Quality (TCEQ) is Dr. Khalid Al-Wali.

1.1. Background

NH_3 emissions have negative consequences on air quality and contribute to the formation of inorganic $PM_{2.5}$, leading to various health issues such as cardiovascular disease, asthma, and respiratory problems (Cheng & Wang-Li, 2019; Pui et al., 2014). The impact of NH_3 on $PM_{2.5}$ formation is especially significant due to its non-linear relationship with ammonium nitrate formation (Zhu et al., 2015a). NH_3 emissions also influence air quality and climate change through several mechanisms, including altering radiative forcing by forming aerosols (Hauglustaine et al., 2014), modifying carbon flux (Pinder et al., 2013), changing the phase of secondary inorganic aerosols (Yang et al., 2018), enhancing light absorption caused by organic aerosols (Huang et al., 2018), and affecting heterogeneous ice nucleation (Kumar et al., 2018). Additionally, NH_3 plays a vital role in the nitrogen cycle by affecting nitrogen-containing compounds like nitrous oxide (N_2O) and nitrogen oxide (NO_x) (Xu Zhenying et al., 2019). Excessive NH_3 deposition can harm delicate ecosystems by causing soil acidification (Howard, 2011), biodiversity loss (Carfrae et al.,

2004), and eutrophication (Paerl et al., 2002). Despite NH_3's significant impact on air quality, climate change, and public health, limited measurements have complicated the investigation of its effects (Momeni et al., 2023). Moreover, the scarcity of relevant observations has resulted in considerable uncertainties in modeling NH_3 and formulating regulatory control plans (Paulot et al., 2014). The lack of reliable information regarding the spatial and temporal distribution of emissions, emission factors, management practices, and farming plans (Zhu et al., 2013, 2015b) has also contributed to uncertainties in bottom-up NH_3 emission inventories.

Inverse modeling methods that utilize observational data are a well-established approach for refining emission inventories and constraining modeling predictions. Remote sensing data, such as NH_3 columns from CrIS instrument, are commonly employed for inverse modeling techniques. While remote sensing data have significantly contributed to our understanding of pollutant spatial patterns, they have limitations, including inadequate spatial and temporal coverage and uncertainties in measurements.

In contrast, chemical transport models (CTM) offer comprehensive data with high spatiotemporal resolution for all species. However, CTM data also carry uncertainties arising from the numerical representation of chemical and physical processes in the atmosphere, as well as uncertainties in modeling inputs. By combining the strengths of modeling data and observations, inverse modeling techniques enhance modeling predictions by effectively addressing uncertainties present in both the predictions and observational data.

Under AQRP project 22-019, UH AQF team used satellite observations from CrIS and IASI to constrain NH_3 emissions over Texas and Gulf of Mexico. By implementing iFDMB inverse modeling technique, updating emissions using satellite data aimed to reduce the uncertainties in NEI NH_3 emissions. UH AQF team further evaluated the updated emissions (posterior emissions) by comparing the updated CMAQ NH_3 values with the satellite observations, as well as surface measurements from Ammonia Monitoring Network (AMoN) monitoring data. Using updated estimates, changes in $PM_{2.5}$ concentrations and inorganic parts were investigated.

In this project, the following tasks were completed:

- Task 1: Preparation of comprehensive satellite, in situ, and modeling data for iFDMB method,

- Task 2: Development of the Reduced-Complexity CMAQ Model (RCCM) for NH_3 and refinement of NH_3 emissions using iFDMB with the combination of CMAQ model and CrIS satellite observations,

- Task 3: Investigation of $PM_{2.5}$ concentrations using the updated emission inventory.

1.2. Overview of report

In Section 2, the modeling setup and inverse modeling technique are described. In Section 3, the results of meteorological fields, satellite data, the evaluation of RCCM, updated emissions, and posterior CMAQ results are presented. Finally, in Section 4, conclusions and recommendations for future work are presented.

2. Modeling Setup and inverse modeling technique

2.1. Modeling setup

2.1.1. Weather Research and Forecasting (WRF) Model

The project started by obtaining meteorological data for chemical transport modeling simulations. WRF simulations were performed to obtain various parameters, including air temperature, specific humidity, surface pressure, U/V components of wind speed, longwave/shortwave radiation flux downwards, and precipitation. These simulations were conducted at a spatial resolution of 12 km over the Texas region. To run the WRF model, meteorological inputs were sourced from the North American Mesoscale Forecast System (NAM) reanalysis datasets (https://rda.ucar.edu/datasets/ds609.0/). The NAM data offered a horizontal resolution of 12 km and provided reanalyzed data at a temporal resolution of 6 hours. This dataset included essential information such as temperature, wind, moisture, soil, and many other relevant parameters that were crucial for the modeling simulations. The WRF domains have sizes of 150×150 for the 12-km domain covering Texas, as depicted in Figure 1. WRF configurations used for simulations are shown in Table 1. The initial and boundary conditions were generated using NAM reanalysis datasets.

10
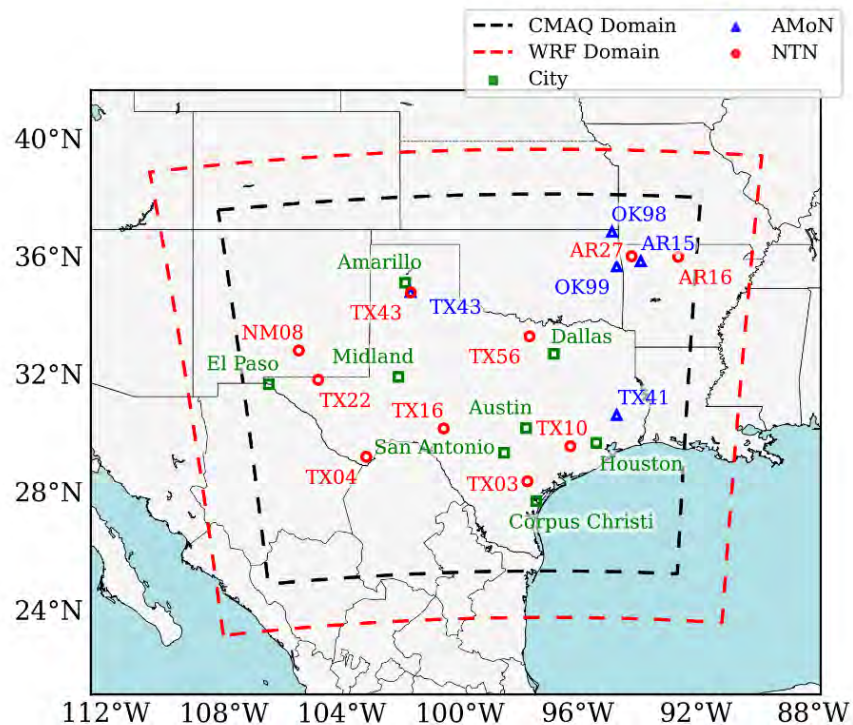
Figure 1: Map of the region of study. AMoN: Ammonia Monitoring Network, NTN: National Trends Network.

Table 1: WRF model configurations for this study.

WRF Version	V4.2
Microphysics	Lin et al. (1983) Scheme
Longwave Radiation	Rapid Radiative Transfer Model for GCMs (RRTMG)
Shortwave Radiation	Rapid Radiative Transfer Model for GCMs (RRTMG)
Surface Layer Option	Pleim-Xu
Land-Surface Option	Unified Noah LSM (Land Surface Model)
Urban Physics	None
Boundary Layer Scheme	ACM2 (Pleim) scheme
Cumulus Cloud Option	Kain-Fritsch

2.1.2. Sparse Matrix Operator Kernel Emissions (SMOKE)

Emissions input for running the CTM was obtained from National Emissions Inventory (NEI). The Environmental Protection Agency (EPA) provided information on the emission of pollutants in the atmosphere through NEI, which offered a comprehensive and detailed estimate of air emissions

of criteria pollutants, criteria precursors, and hazardous air pollutants from various air emissions sources, including NEI point sources, NEI nonpoint sources, NEI on-road sources, and NEI nonroad sources. For this project, the NEI modeling platform was utilized, incorporating the NEI emission inventory and Sparse Matrix Operator Kernel Emissions (SMOKE) to spatially and temporally allocate the emission values to modeling grids. Emissions from natural sources were estimated using the Biogenic Emissions Inventory System (BEIS3). As for mobile emissions, they were processed based on the 2017 Motor Vehicle Emission Simulator (MOVES) output within the NEI package. The NEI modeling platform from the year 2017 was employed to produce emissions at a 12km spatial resolution for Texas throughout the entire year of 2019. While the NEI does not account for biogenic oceanic emissions, we turned to the Emissions Database for Global Atmospheric Research (EDGAR) to quantify these emissions for the Gulf of Mexico region. It's imperative to note that biogenic oceanic emissions primarily arise from Biological Nitrogen Fixation (BNF). BNF refers to the conversion of dissolved nitrogen (N_2) gas into bioavailable forms, such as NH_3 and NH_4^+ by marine nitrogen-fixing organisms known as diazotrophs (Holland & Turekian, 2014).

2.1.3. CMAQ

Meteorological inputs and emissions were used for atmospheric chemistry simulations using CMAQ. CMAQ is a chemical transport model developed and maintained by the US EPA that comprehensively predicts the most important processes affecting the chemistry of the atmosphere. CMAQ comprehensively simulates the chemistry of the atmosphere by considering processes such as advection, diffusion, and wet and dry deposition, and chemical reactions are represented within this model. By using an extensive database of atmospheric chemical reactions, CMAQ predicts the chemical production and loss of hundreds of pollutants to demonstrate the chemistry of the atmosphere. The following configurations were used for CMAQ. Major CMAQ configurations are shown in Table 2.

2.2. Inverse modeling setup

2.2.1. Satellite data

To refine NH_3 emissions for 2019, the CrIS satellite was employed. However, a data gap between March 25 and August 12 due to the absence of CrIS observations posed a challenge to using CrIS

satellite data exclusively for revising NH_3 emissions for the entire year. To address this, the UH AQF team incorporated IASI observations to fill in the missing data.

Table 2: Major CMAQ configurations.

CMAQ version	V5.0.1
Chemical Mechanism	cb05tucl_ae5_aq: Carbon-Bond version 5 (CB05) gas-phase mechanism with active chlorine chemistry, updated toluene mechanism, fifth-generation CMAQ aerosol mechanism with sea salt, aqueous/cloud chemistry
Lightning NOx emission	Included by using inline code
Horizontal advection	Yamartino Scheme
Vertical advection	WRF omega formula
Horizontal mixing/diffusion	Multiscale
Vertical mixing/diffusion	Asymmetric Convective Model version 2
Chemistry solver	Euler Backward Iterative (EBI) optimized for the Carbon Bond-05 mechanism
Aerosol physics and chemistry	Aerosol module version 5 (AERO5) for sea salt and thermodynamics
Cloud Option	Asymmetric Convective Model (ACM)
Initial Condition (IC) / Boundary Condition (BC)	Default static profiles

CrIS

To constrain emissions using satellite data, CrIS and IASI satellite observation for NH_3 were used. The CrIS instrument is an infrared sounder onboard the sun-synchronous satellite Suomi National Polar-orbiting Partnership (SNPP) mission launched in October 2011. It had a mean local daytime overpass time of 13:30 and a mean local nighttime overpass time of 01:30. CrIS provided an across-track scanning swath width of 2,200 km and a nadir spatial resolution of 14 km (Dammers et al., 2017). To prepare the CrIS satellite observation for this project, a CrIS observation operator developed by Momeni et al. (2023) was employed. The subsequent sections explained the CrIS observation operator.

IASI

The IASI instruments on the MetOp-A and -B satellites follow sun-synchronous orbits and execute overpasses at 09:30 and 21:30 local standard time (LST). The observational swath of both IASI instruments spans over 2,000 km, featuring a pixel footprint of 12 km in diameter at nadir viewing angles (Dammers et al., 2019). This study harnesses both daytime and nighttime observations from IASI. A comparison of IASI data with ground-based Fourier transform infrared (FTIR) observations revealed a correlation coefficient (r) of 0.8 and a slope of 0.73 (Dammers et al., 2016). As documented by van Damme et al. (2015), a commendable concordance exists between IASI NH_3 data and ground observations sourced from the Ammonia Monitoring Network (AMoN). For this investigation, any pixels demonstrating a cloud fraction exceeding 0.3 were eliminated.

2.2.2. Inverse modeling technique: iFDMB

The iFDMB inverse modeling was employed to refine the NH_3 emission inventories as implemented in Momeni et al. (2023). In the iFDMB, a-priori concentrations retrieved using a forward model were used to linearize the sensitivity of the column density (Ω) to NH_3 emissions (E) at every grid point. Then, top-down emissions (E_t) were calculated at each iteration as follows:

$$E_t = E_a(1 + \frac{1}{\beta}\frac{\Omega_o - \Omega_a}{\Omega_a}), \tag{1}$$

where E_a presents a-priori emissions from the previous iteration, Ω_o the observed column, Ω_a the simulated column, and β the initial sensitivity given as:

$$\beta = \frac{\Delta\Omega/\Omega}{\Delta E/E}. \tag{2}$$

A perturbation of 20% to the a-priori emissions, E, was applied in each grid to determine the initial sensitivity. The iteration process was repeated until the normalized mean difference (NMD) of new emissions with respect to the emissions calculated from the last iteration was less than 1% or 2%. In this study, NMD of 2% is has been employed.

2.2.3. Reduced-Complexity CMAQ Model (RCCM) for NH_3

The iFDMB technique performs multiple model simulations to converge on the final results. To reduce the computational cost, an RCCM was employed to simulate NH_3. In the RCCM, NH_3 and NH_4^+ are considered as two tracer pollutants of the model and all other species' chemical processes are turned off. The developed RCCM included dry and wet deposition, the transport of NH_3 and NH_4^+, and NH_x partitioning; the subroutine of ISORROPIA-II in the aerosol module calculates the gas-particle partitioning of NH_3 and NH_4^+. While running RCCM, the hourly sulfate (SO_4^{2-}), nitric acid (HNO_3), nitrate (NO^{-3}), chloride (Cl), sodium (NA), hydrochloric acid (HCl) concentrations are read from archived standard CMAQ simulation offline files.

2.2.4. Observation Operator

To employ the iFDMB technique to improve NH_3 emissions, satellite data from the CrIS and IASI satellite observation were used. For operating the iFDMB, only valid pixels with quality flag values exceeding 3 were selected. To apply the iFDMB inverse modeling and to also compare model estimates to satellite observations, the vertical column of the model was calculated by summing a modeled partial column from Herron-Thorpe et al. (2010), which is in molecule cm^{-2}, as follows:

$$VCD_i = \frac{c_i}{10^6} \times \frac{L_{Ti} \times P_i \times N_A}{R \times T_i}, \tag{3}$$

where the i index is the level number, c the concertation of NH_3 in ppmv, L_{Ti} the model layer thickness, P the pressure in pascals, N_A Avogadro's number, R the molar gas constant, and T the temperature in Kelvins. By substituting the equation of state and the hydrostatic equation into Equation (3), the vertical column density was given by:

$$VCD_i = -c_i \times \Delta P_i \times 2.119 \times 10^{14}. \tag{4}$$

For CrIS, since the averaging kernel is provided, the column density was calculated by using the observational operator, H, to estimate the model NH_3 profile:

$$Hc = c_a + A(Mc - c_a), \tag{5}$$

15

where c is the model-estimated NH$_3$ profile, M a matrix that maps the space of the model to the space of CrIS, A the averaging kernel, and c_a is the a-priori NH$_3$ profile, the total vertical column density of the model is calculated as

$$VCD = \sum_i VCD_i. \tag{6}$$

2.2.5. A-priori emissions

Quarterly a-priori NH$_3$ emissions are depicted in Figure 2. It is important to note that the months are represented with abbreviations as follows: January, February, and March (JFM); April, May, and June (AMJ); July, August, and September (JAS); and October, November, and December (OND).The prior emissions provided by NEI display spatio-temporal variation over Texas. The highest emission values are observed in Northern Texas, where agricultural land use is more condensed, as shown in Figure 3. In terms of seasonal variation, JAS has the highest values while OND is the least. In the rest of Texas, higher emissions values are also associated with the location of agricultural practices. In the Gulf of Mexico region, the ammonia emissions exhibit minimal values, with certain locales approaching a near-zero magnitude. Furthermore, no significant spatio-temporal fluctuations in these emissions are evident across sequential quarters.

3. Posterior evaluation

The posterior evaluation entails a comparative analysis of the updated model simulations against observational datasets from satellite retrievals and surface measurements. In order to assess the efficiency of the model, a comparison was made between the posterior and prior estimates versus data from the CrIS/IASI satellites. Due to the availability of the data, different datasets were used. For instance, for the months of January, February, and March (JFM), the CrIS satellite had the most available data. However, for the months of July, August, and September (JAS), both CrIS and IASI data were utilized.
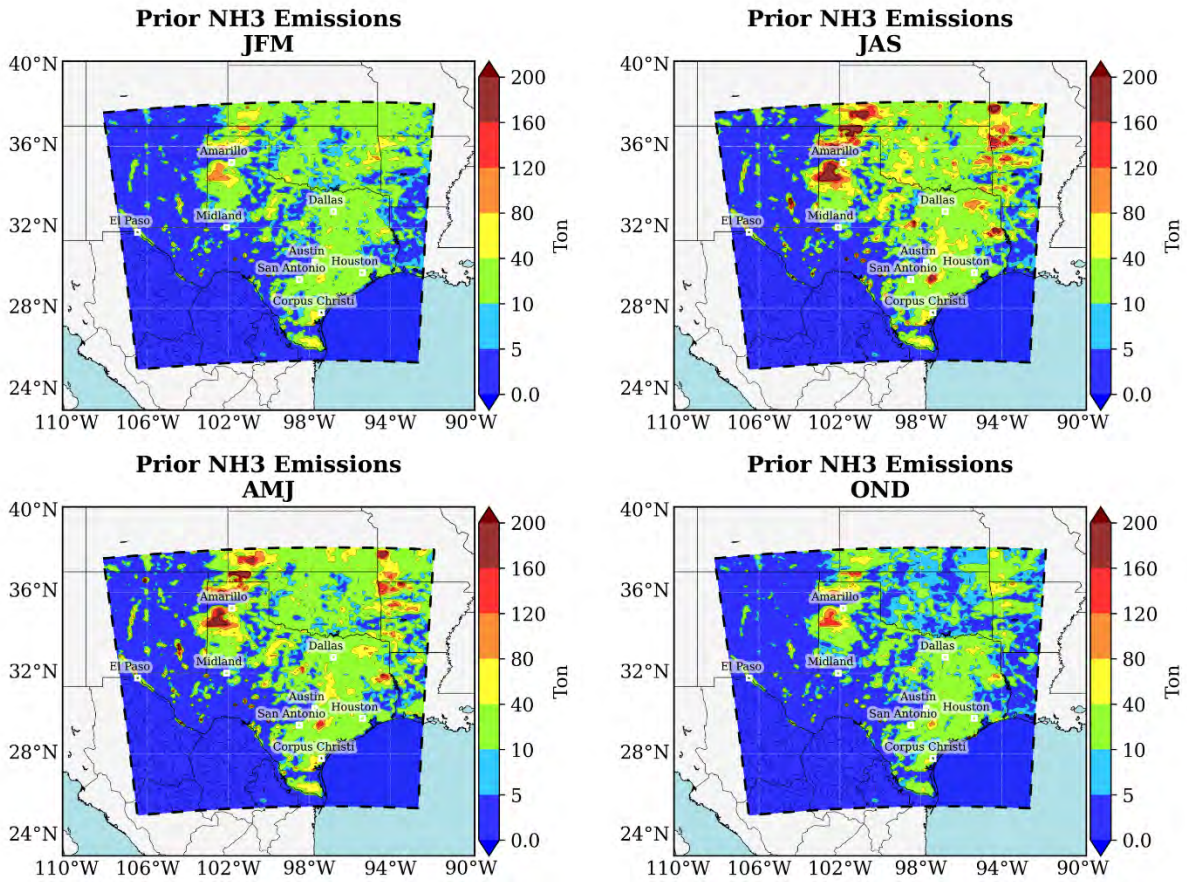
Figure 2: Quarterly a-priori NH₃ emissions.
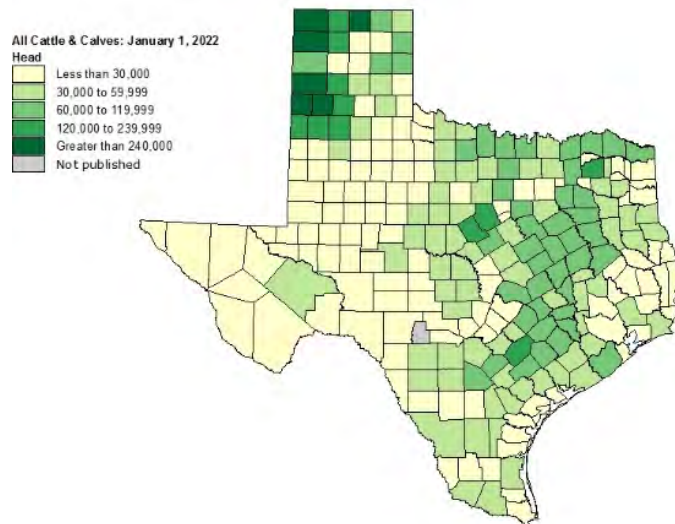
Figure 3: County Estimate Map – Cattle (nass.usda.gov).

17

The posterior emissions are evaluated by comparing the model simulation from updated emissions with surface measurements. The Ammonia Monitoring Network from the National Atmospheric Deposition Program (NADP) is a program that monitors and measures the atmospheric ammonia NH_3 concentrations and deposition of NH_4^+ in the United States. The available data for ammonia are bi-weekly averages. The bi-weekly measurement of ammonia in the Ammonia Monitoring Network (AMoN) means that air samples are collected and analyzed at each monitoring site every two weeks. Since the ammonia network provides bi-weekly averages, the bi-weekly averages of the model were used for a fair apple-to-apple comparison during the evaluation process. The unit of measure for ammonia concentration is micrograms per cubic meter (µg/m³). To convert this measurement to ppb, the pressure, and temperature of the nearest point to the station within the domain are taken into account. For the comparison, 6 active stations were employed over the domain with IDs of AR03, AR09, AR15, OK98, OK99, TX41, and TX43, from which the data is downloadable on the NADP website as shown in Figure 1.

For NH_4^+ deposition, wet deposition values are available from the NADP's National Trends Network (NTN), which measures total weekly wet deposition. For an apple-to-apple wet deposition comparison, the weekly averages of the wet deposition in the model were calculated. For evaluation against the NH_4^+ wet deposition, precipitation bias adjustment (PBA) is also applied. The precipitation bias adjustment scales the simulated deposition by the ratio between measured and simulated precipitation to reduce errors in the precipitation estimates from the meteorological model:

$$PBA = \frac{\sum p_o}{\sum p_m} \sum WD_m$$

Which, $\sum p_o$ is the monthly/quarterly total accumulated observed precipitation, $\sum p_m$ is the monthly/quarterly total accumulated modeled precipitation, $\sum WD_m$ represents the monthly/ quarterly accumulated wet deposition estimate from the model. For the evaluation, 11 stations were used over the domain with IDs of AR03, AR16, AR27, NM08, TX03, TX04, TX10, TX16, TX22, TX43 and TX56 as shown in Figure 1.

4. Results

4.1. Meteorological fields

Meteorological fields were produced using WRFv4.2 and NAM reanalysis data. Spatial plots of monthly average temperature and wind velocity are presented in Figure 4.
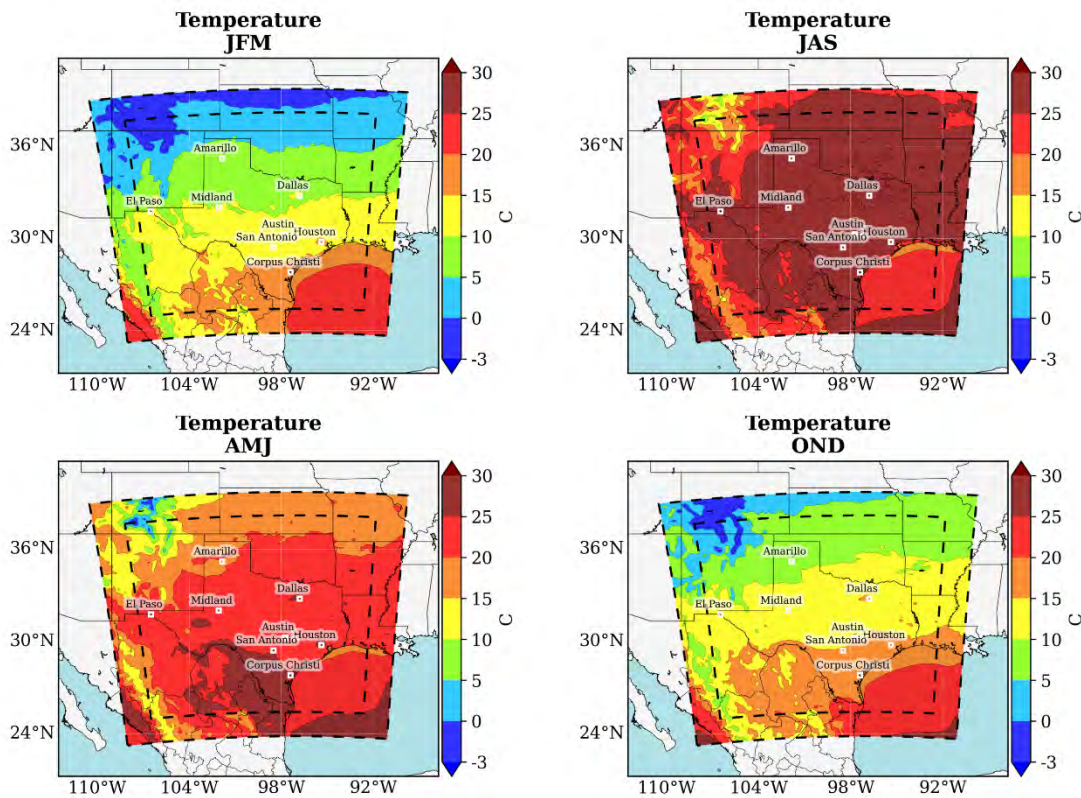
Figure 4: WRF monthly average temperature for 2019.

The UH AQF team evaluated the outputs of the WRF model using data collected from the Meteorological Assimilation Data Ingest System (MADIS) stations in Texas for the year 2019 (https://madis.ncep.noaa.gov/index.shtml). The focus of this evaluation was on three key meteorological variables: U10 (east-west wind component at 10 meters above the ground), V10 (north-south wind component at 10 meters above the ground), and T2 (2-meter air temperature). The primary objective was to assess how well the WRF model captured the atmospheric conditions over Texas during the specified time frame. To conduct the evaluation, the UH AQF team obtained the WRF model hourly outputs and corresponding observations from the MADIS network for the entire year of 2019 over Texas.

19

The evaluation was performed through a series of statistical analyses, which involved comparing the WRF model outputs against the observed data from the MADIS stations. The statistical metrics used for the comparison include Mean Absolute Error (MAE), Root Mean Square Error (RMSE), correlation coefficients and index of agreement (IOA). These metrics allow us to quantify the discrepancies between the model outputs and the observations and assess the overall agreement between the two datasets. The evaluation process involves comparing the average value of all stations, at each specific time, to the nearest grid point on the WRF model's grid. This comparison allows us to assess how well the WRF model's output represents the observed data from the meteorological stations.

The results of the evaluation shown in Figure 5 indicate that the WRF model generally captured the spatial and temporal variations of U10, V10, and T2 over Texas during the year 2019. However, some discrepancies were observed between the model outputs and the MADIS observations. The statistical values are shown in Table 3. For the U10 component, the WRF model showed a relatively good agreement with the MADIS data in most regions of Texas, with MAE and RMSE values within acceptable ranges. The correlation coefficients indicated a significant positive relationship between the model and observation data. Similarly, for the V10 component, the WRF model performed reasonably well and much better than U10, displaying coherent patterns with the MADIS observations. The statistical analysis revealed relatively low MAE and RMSE values, indicating a satisfactory performance of the model in capturing the north-south wind component.

Table 3: Statistical values for WRF evaluation (R and IOA are unitless).

Variable	R	IOA	RMSE	MAE	Errors Unit
U10	0.66	0.79	1.89	1.51	m/s
V10	0.78	0.86	2.19	1.74	m/s
T2	0.95	0.96	2.94	2.26	C

Regarding the T2 variable, the WRF model demonstrated a relatively strong performance in reproducing the 2-meter air temperature across Texas. The MAE and RMSE values were generally low, and the correlation coefficients showed a strong positive relationship between the model outputs and the MADIS observations.

20

The evaluation of WRF outputs with MADIS stations in Texas for the year 2019 provided valuable insights into the model's performance for U10, V10, and T2 variables. Overall, the WRF model showed a promising ability to simulate atmospheric conditions over the region by having IOA of 0.79, 0.86 and 0.96 for U10, V10 and T2, respectively.
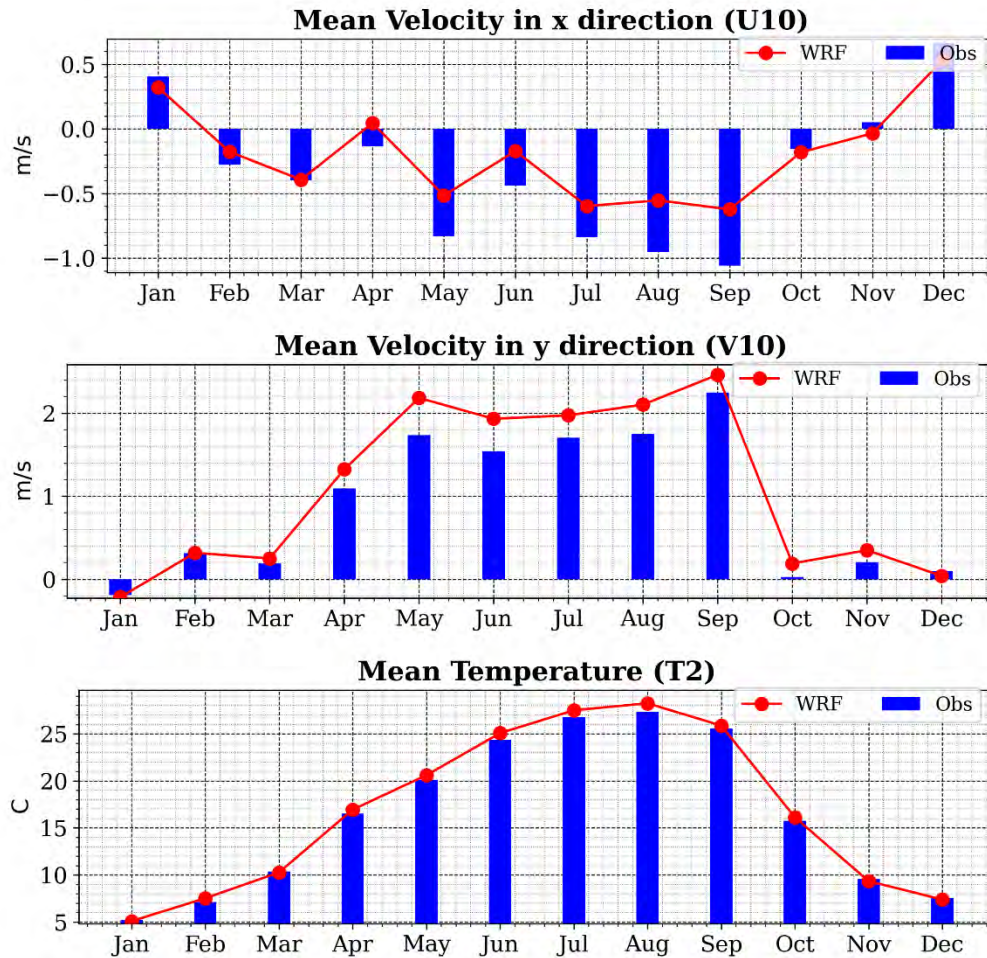
Figure 5: Time series for U10, V10, and T2 evaluation, monthly averages.

4.2. Satellite data

As previously mentioned, in this project, comprehensive datasets extracted from two distinct satellite sources, CrIS and IASI, were leveraged. It's important to point out that the IASI satellite dataset poses a challenge due to the absence of an averaging kernel, an essential component for refining data reliability and consistency. Additionally, the CrIS satellite's data retrieval presents partial coverage, restricting the comprehensiveness of our research domain.

Despite these constraints, a robust methodological adaptation has been implemented to bolster the research. The emissions inventory has been adjusted, taking advantage of the density column data available from both satellites. This approach has enabled the refinement of emission values accurately, effectively overcoming the potential limitations posed by individual satellite data sources.

Figure 6 illustrates the spatial distribution of the NH_3 column density over Texas and the Gulf of Mexico for 2019, divided into four quarters. It is noteworthy that the JFM and OND periods are monitored by the CrIS satellite, while the AMJ period is covered by the IASI satellite. Additionally, the first half of the JAS period is observed by IASI, with the remaining part of AS observed by CrIS.

As depicted in Figure 6, spatial variation in NH_3 values has been displayed by satellite column density data. Hotspots of satellite NH_3 values have been observed over regions with expected high NH_3 emissions, such as areas with dense agricultural activities and around major cities. The significance of high NH_3 values in regions located in the Northwestern and Southeastern parts has been explored in this work.

4.3. Top-down estimation of NH_3 emissions

By capitalizing on the strengths of both satellites data sets, the emission inventory has been successfully refined, reinforcing the reliability of the research findings.

4.3.1. Changes in emissions over land/sea

Figure 7 illustrates the spatial distribution of quarterly averaged NH_3 emissions, delineating both the a-priori (before) and a-posteriori (after) emissions, following the application of the iFDMB method, as well as highlighting the changes in NH_3 emissions across the study domain. Through the implementation of the iFDMB method, a notable increase in emissions has been observed in the regions encompassing Northwestern and Southeastern Texas and extending over the Gulf of Mexico. These increases are particularly significant in areas with anticipated higher emissions, signaling a potential underestimation of prior emissions within these specific regions.
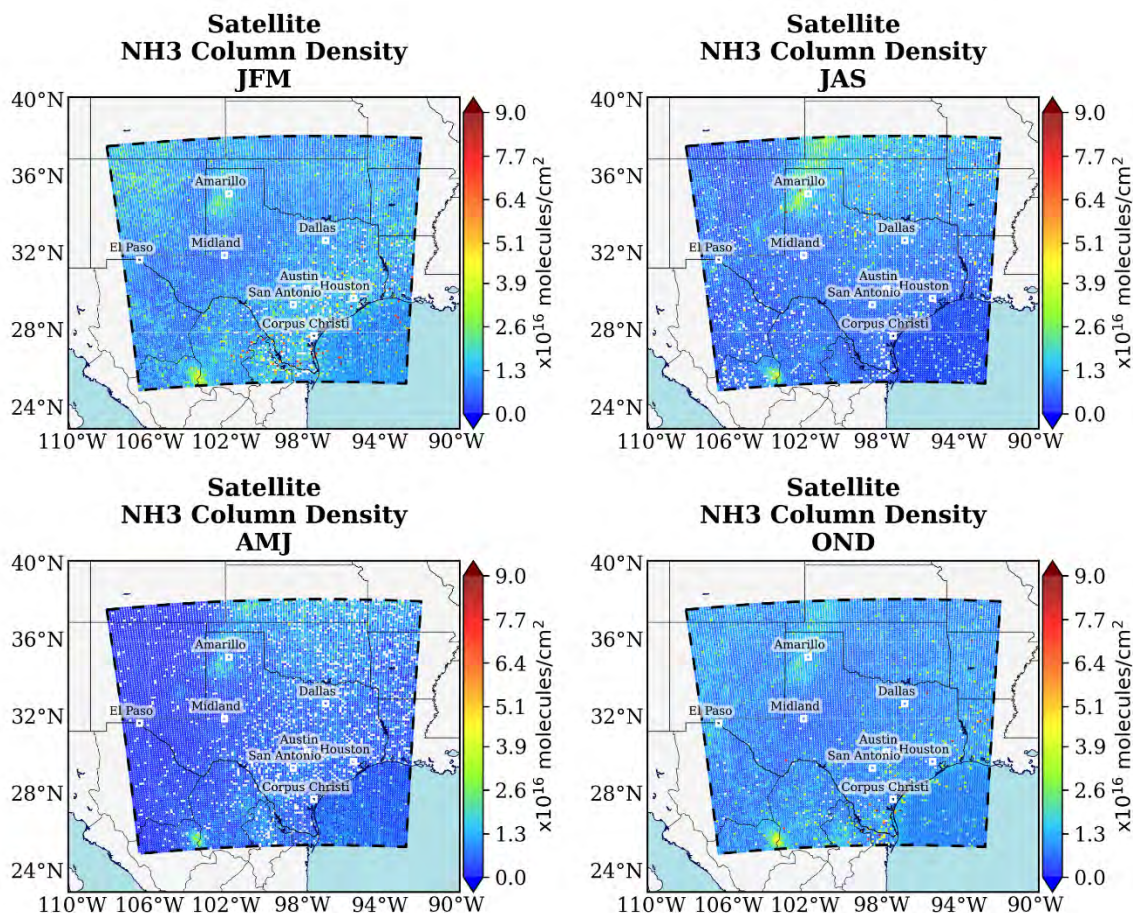
Figure 6: The spatial distribution of satellite data over Texas and the Gulf of Mexico for 2019.

In the Northwestern part of Texas, elevated NH_3 emissions are a predictable phenomenon, largely attributable to the prevalence of dense agricultural practices that inherently contribute to higher emission levels. Furthermore, the high NH₃ levels in Southeast Texas match what previous studies have shown, confirming that our findings are consistent with past research. The elucidation of these spatial patterns enhances our understanding of regional emission dynamics, providing invaluable insights for environmental monitoring and policy implementation.

Increasing and changing NH_3 emission levels over the Gulf of Mexico are of great importance as they suggest the underestimation of NH_3 emissions in NEI. The ocean plays a significant role in natural emissions, contributing to over 40% of all natural emissions and 15% of global emissions, making it the largest natural source of emissions (Paulot et al., 2015). Biological nitrogen fixation (BNF) is the process in which dissolved nitrogen (N_2) gas is converted into bioavailable nitrate

(NO_3^-) and ammonium (NH_4^+) by marine nitrogen fixers (diazotrophs) (Holland & Turekian, 2014). Ocean emissions are positively influenced by concentrations of nitrate and ammonium in seawater, as well as temperature, pH, and salinity (Paulot et al., 2015). Furthermore, emissions can also arise from shipping and oil-related operations over the ocean (Woo et al., 2020).

As shown in Figure 7, after the implementation of inverse modeling, emissions values increase across Texas. During JFM, there is an increase of over 60 tons in emissions in the Northwestern parts of Texas, and an over 20 tons increase in the Southeastern areas, with the emissions over the Gulf of Mexico increasing by more than 10 tons. Interestingly, the same increase is observed during OND. In contrast, during AMJ, the increase in emissions is comparatively lower, with over 20 tons in Northwestern Texas and over 10 tons in the Southeastern regions, while the Gulf of Mexico sees an increase of more than 10 tons. However, in JAS, the emissions in Northwestern Texas increase by more than 40 tons and by more than 10 tons in the Southeastern regions, whereas the Gulf of Mexico experiences an increase of more than 1 ton.

A significant point to be noted across all quartiles and annual updated emissions is that a noticeable increase in ammonia emission levels is observed over Texas. The coastline and extending over the Gulf of Mexico, demonstrates significantly elevated emission levels in comparison to the a-priori emissions. Contrary to NEI estimates, which indicated low emission values for this region and the Gulf of Mexico, the adjusted emissions data display a substantial increase. The updated emissions derived through our inverse modeling suggest the necessity of a thorough reevaluation of ammonia emissions from the Gulf of Mexico.

It is worth to note that biomass burning happens in Texas from February to September, especially in Southeastern Texas (Zhang et al., 2014). The high values in updated ammonia emissions in Southeastern Texas could potentially be correlated with this biomass burning. However, a comprehensive investigation is essential to confirm this correlation.

These critical results pose substantial implications for the understanding of regional emission dynamics, and they hold the potential to profoundly influence strategies related to environmental monitoring and policy-making. Our findings underscore the need for adaptive and responsive

strategies to accurately quantify and manage ammonia emissions, thereby contributing to a more sustainable and informed environmental framework.
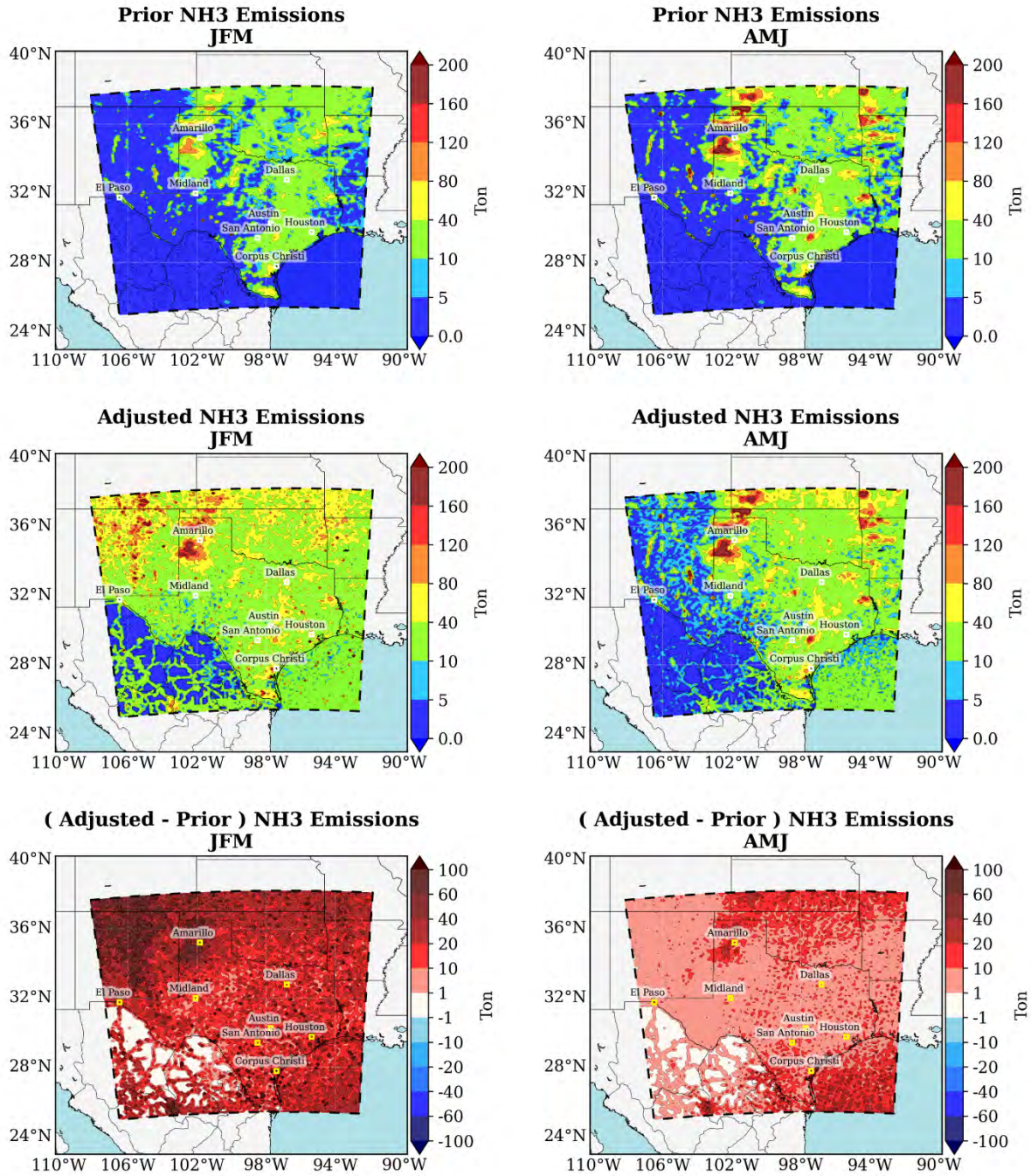
Figure 7 - continue
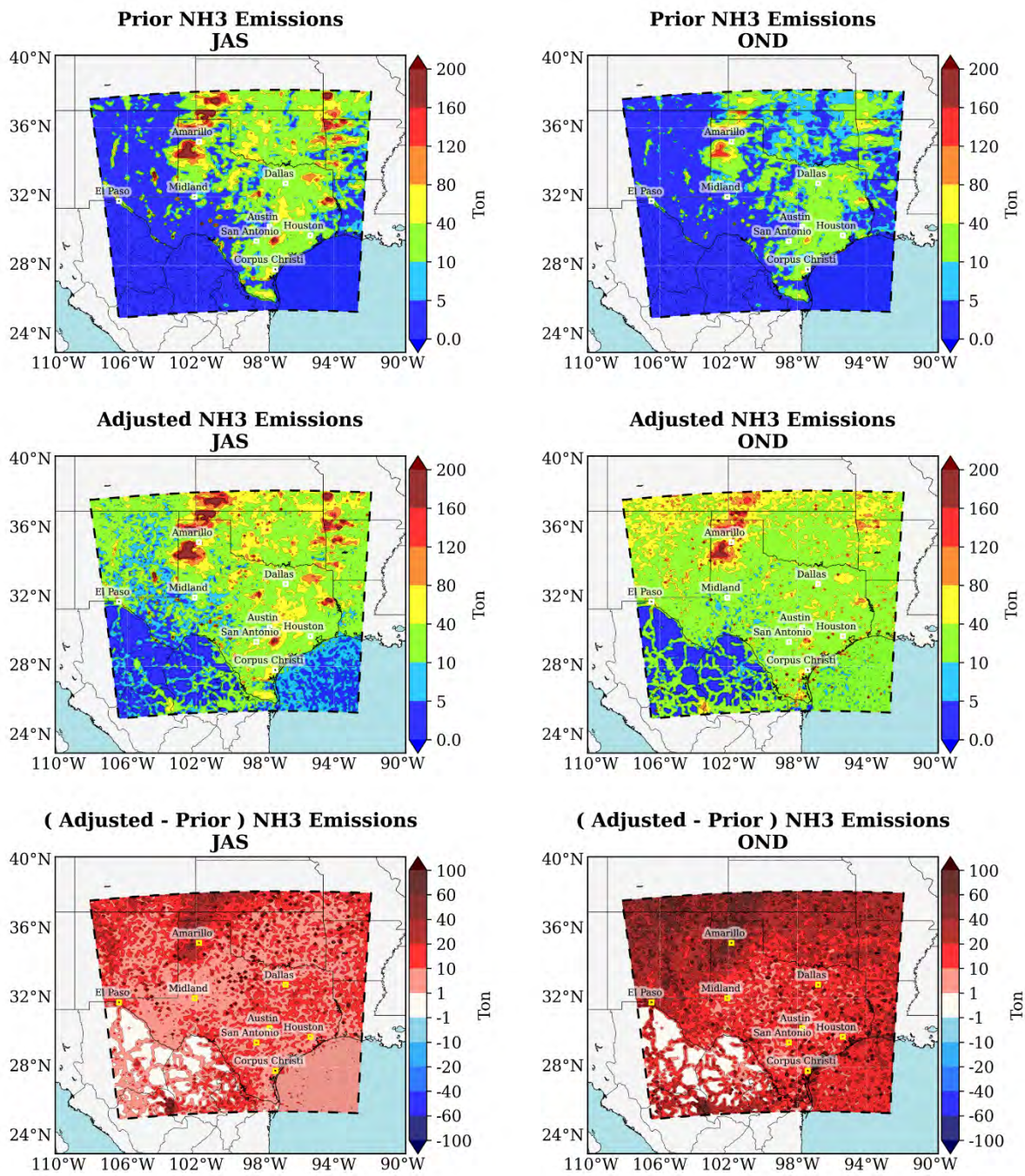
Figure 7 - continue
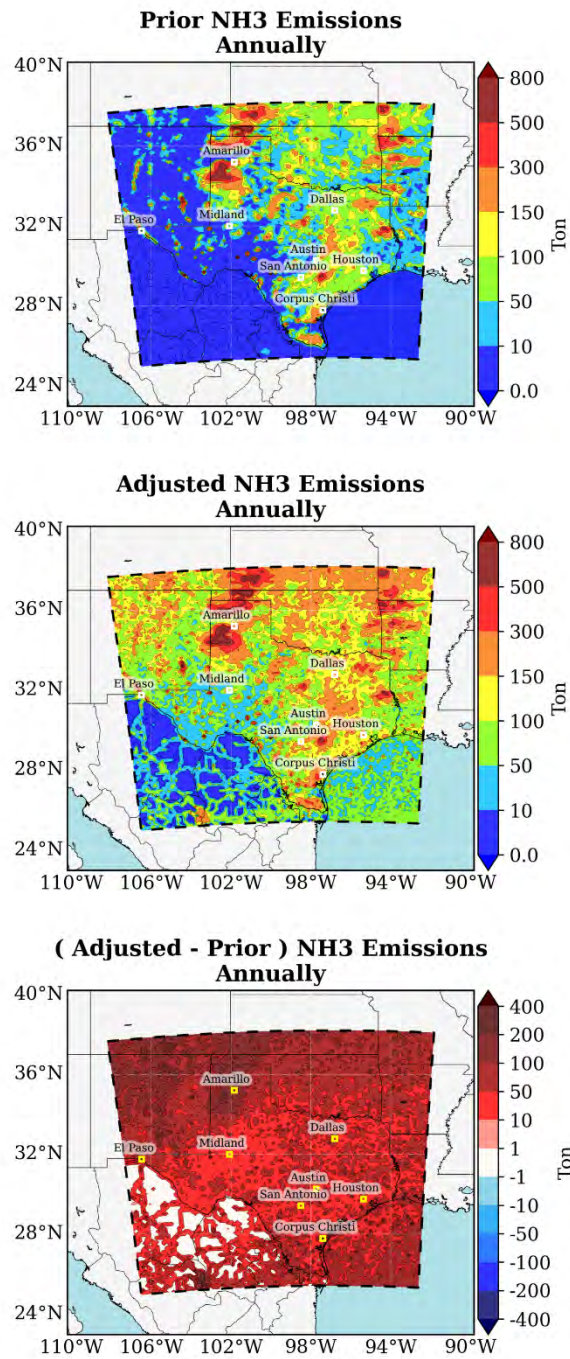
Figure 7: the spatial quarterly distribution for a-priori and a-posteriori NH$_3$ emissions.

4.3.2. Posterior NH_3 concentrations

Figure 8 represents the a-priori and a-posteriori NH_3 concentrations and the difference between the a-posteriori and a-priori NH_3 concentrations. For months of January, February, and March (JFM), there's a notable increase in NH_3 concentrations, corresponding to the previously shown increase in NH_3 emissions. Northwestern Texas exhibits an increase of more than 4 parts per billion (ppb) in NH_3 concentrations, while the rest of Texas shows an increase of more than 1 ppb. Increased NH_3 concentrations in Northwestern Texas reflect findings observed in earlier surface measurements. Interestingly, the a-priori NH_3 concentrations in Northwestern Texas were not as high, ranging between 3-4 ppb. The considerable increase in a-posteriori values underscores the underestimation in the NEI and demonstrates the efficacy of the inverse modeling technique in adjusting the emissions.

Notably, the rise in NH_3 concentrations over the Gulf of Mexico in the a-posteriori results is highly significant, given that the emissions over the Gulf of Mexico are typically very low. With the updated emissions, NH_3 concentrations increase by more than 1 ppb, indicating that the inverse modeling technique successfully reproduces NH_3 concentrations over the ocean caused by biological nitrogen fixation and maritime activities, such as shipping and oil operations. These values are not observed when using NEI emissions. Moreover, the high levels of NH_3 during this period suggest intensified activities producing NH_3.

During the AMJ period, a rise in a-posteriori NH_3 concentrations is observed when compared to the a-priori values. Notably, Northwestern Texas experienced a significant increase in a-posteriori NH_3 concentrations, with values rising between 1-2 ppb. In contrast, the rest of Texas saw a more modest increase in NH_3 concentrations, ranging between 0.3-1 ppb, compared to the a-priori concentration. Substantial increases were also observed for a-posteriori NH_3 concentrations over the Gulf of Mexico, where the a-posteriori concentrations exhibited an increase of 1-2 ppb, mirroring the trend seen during the JFM period. It's important to highlight that for the AMJ period, the IASI satellite data were used to refine the emissions, while the CrIS satellite data were utilized for the JFM period. These discrepancies in updates between the JFM and AMJ periods could be attributed to both quarterly variances and the differences in values reported by these two satellites. In addition, the high NH_3 concentrations measured during this period by AMoN, coupled with the

lower IASI-constrained values, suggest a possible underestimation of the values reported by the IASI during this period.
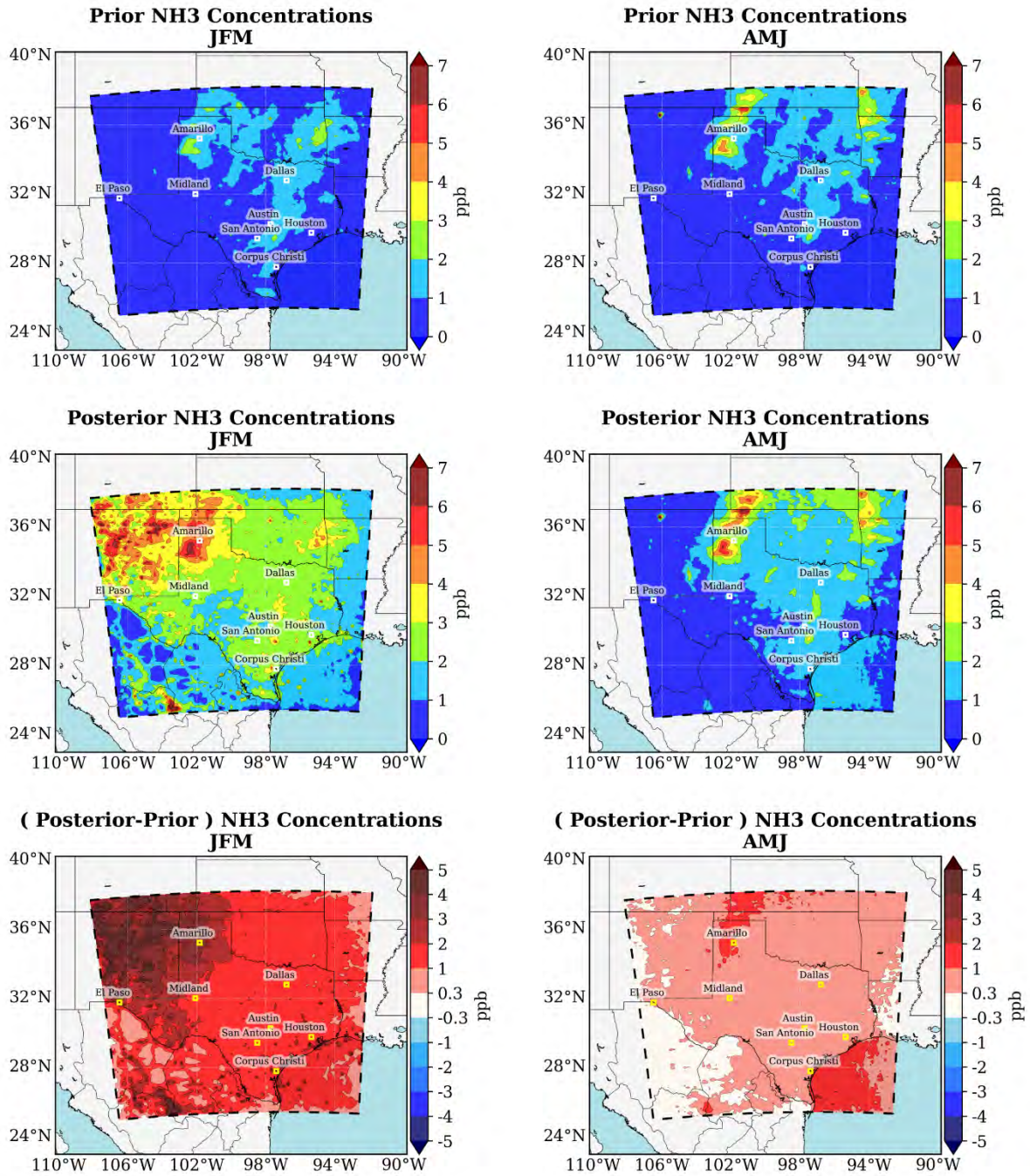
Figure 8 - continue
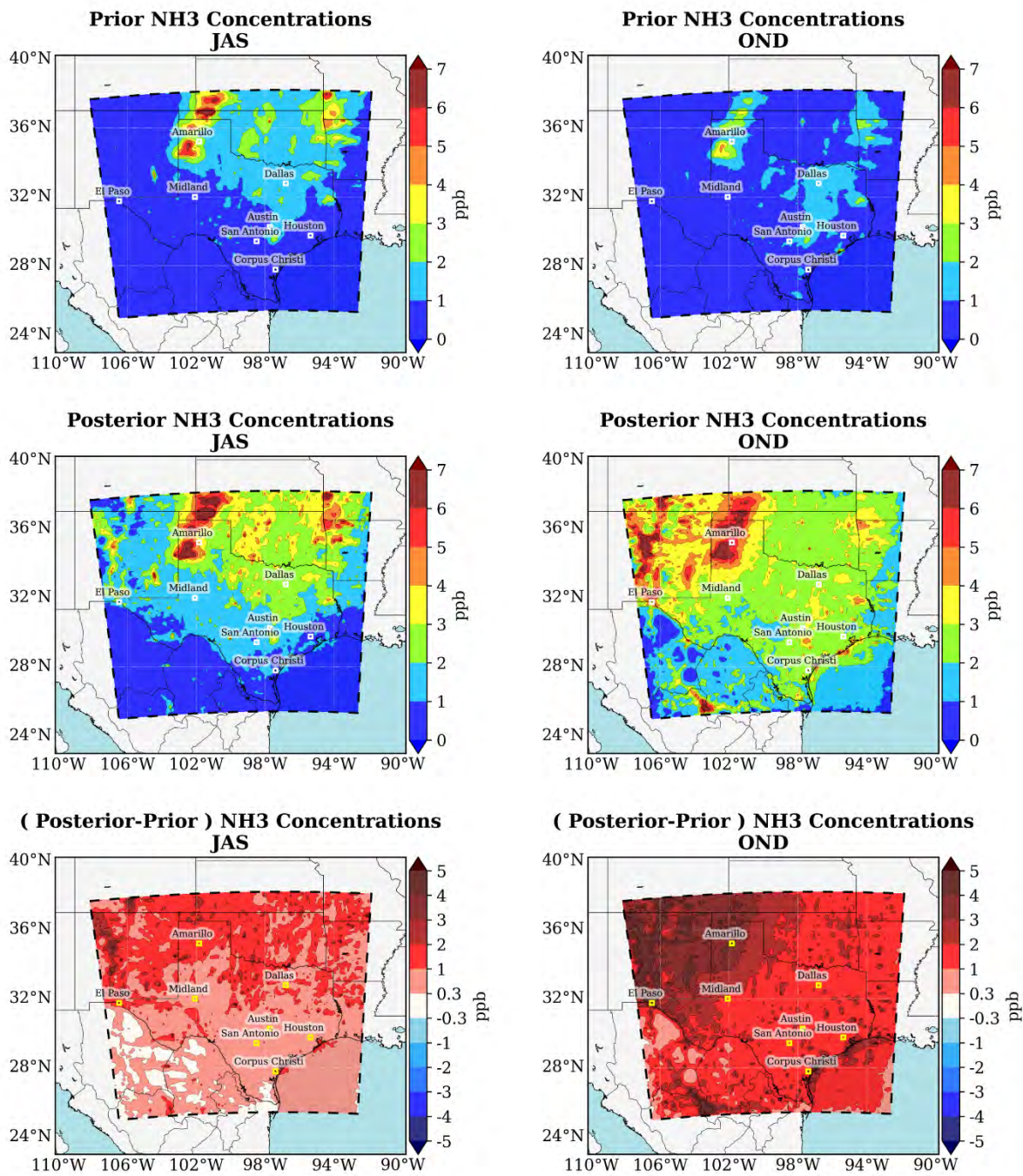
Figure 8 - continue
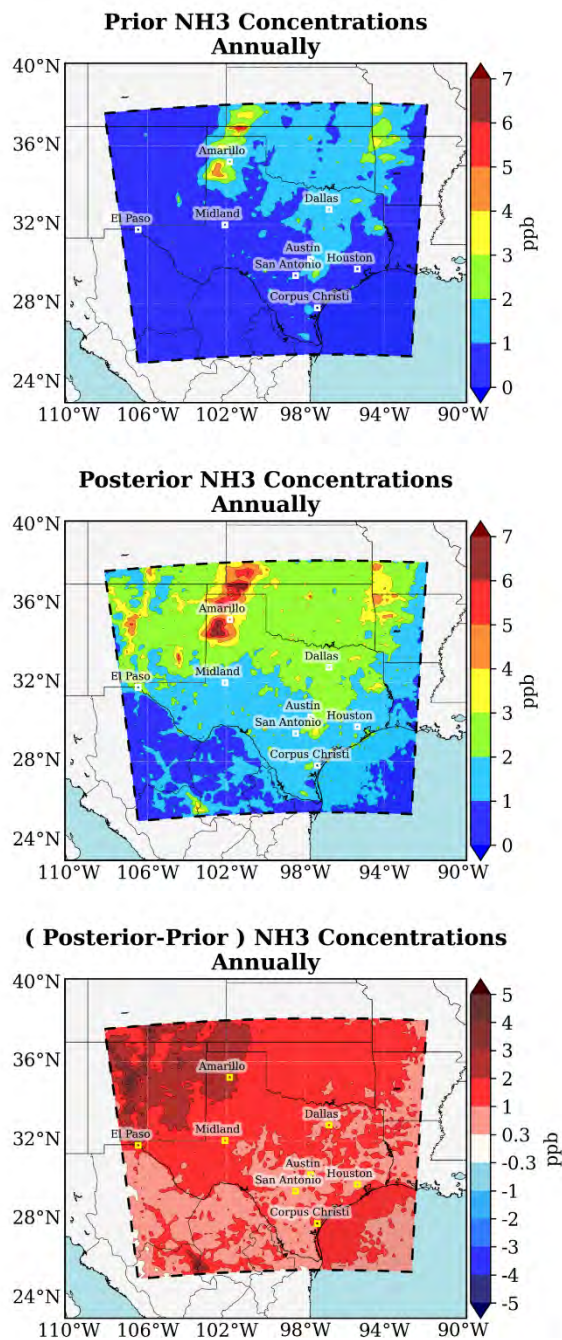
Figure 8: The spatial quarterly/annually averaged distribution for a-priori and a-posteriori NH₃ concentrations and its difference.

During the JAS period, a-posteriori NH_3 concentrations in Northern Texas exhibited an increase of 1-2 ppb, while the rest of Texas showed a more modest rise of 0.3-1 ppb. Over the Gulf of Mexico, NH_3 concentrations increased between 0.3-1 ppb. A key finding was the identification of two hotspots for NH_3 concentrations over the ocean, near the shoreline. These localized increases underscore the potential significance of shipping activities in those areas.

In the OND period, significant increases in a-posteriori values were observed, similar to those in the JFM period. For OND, NH_3 concentrations surged by more than 4 ppb. Elsewhere in Texas, NH_3 concentrations increased by 1-2 ppb, while sporadic regions across Texas saw an increase of 2-3 ppb. Notably, these areas of increase correlate with the dense agricultural land use as illustrated in Figure 3. Over the Gulf of Mexico, NH_3 concentrations increased by 2-3 ppb due to biological nitrogen fixation and maritime and oil industrial activities, with hotspots along the shoreline showing an increase of 3-4 ppb, likely indicating maritime activities in these regions.

On the annual average concentrations, NH_3 concentrations across Texas have shown an increase. The most substantial increase occurred in the Northwestern regions, where values rose between 3-4 ppb. In the rest of Texas, including most of the northern parts and some eastern areas, the increase ranged between 1-2 ppb. Over the Gulf of Mexico, the 1-2 ppb increase in NH_3 concentrations highlights the notable role of sources over the ocean, likely related to biological nitrogen fixation and maritime and oil industrial activities.

4.4. Spatial distribution of inorganic species

Given that alterations in NH_3 emissions can significantly impact the concentrations of inorganic PM2.5, it is crucial to examine variations in inorganic species such as ammonium (NH_4^+), sulfate (SO_4^{2-}), and nitrate (NO_3^-). In the following section, the changes in these inorganic species as a result of the updated ammonia emissions are presented.

4.4.1. Ammonium concentrations

Figure 9 displays the spatial distribution of NH_4^+, simulated using a-posteriori and a-priori NH_3 emission. By considering the direct relationship between NH_3 and NH_4^+ ($NH_3 \rightleftharpoons NH_4^+$), NH_4^+ is expected to vary directly as a result of changes in NH_3 concentrations.
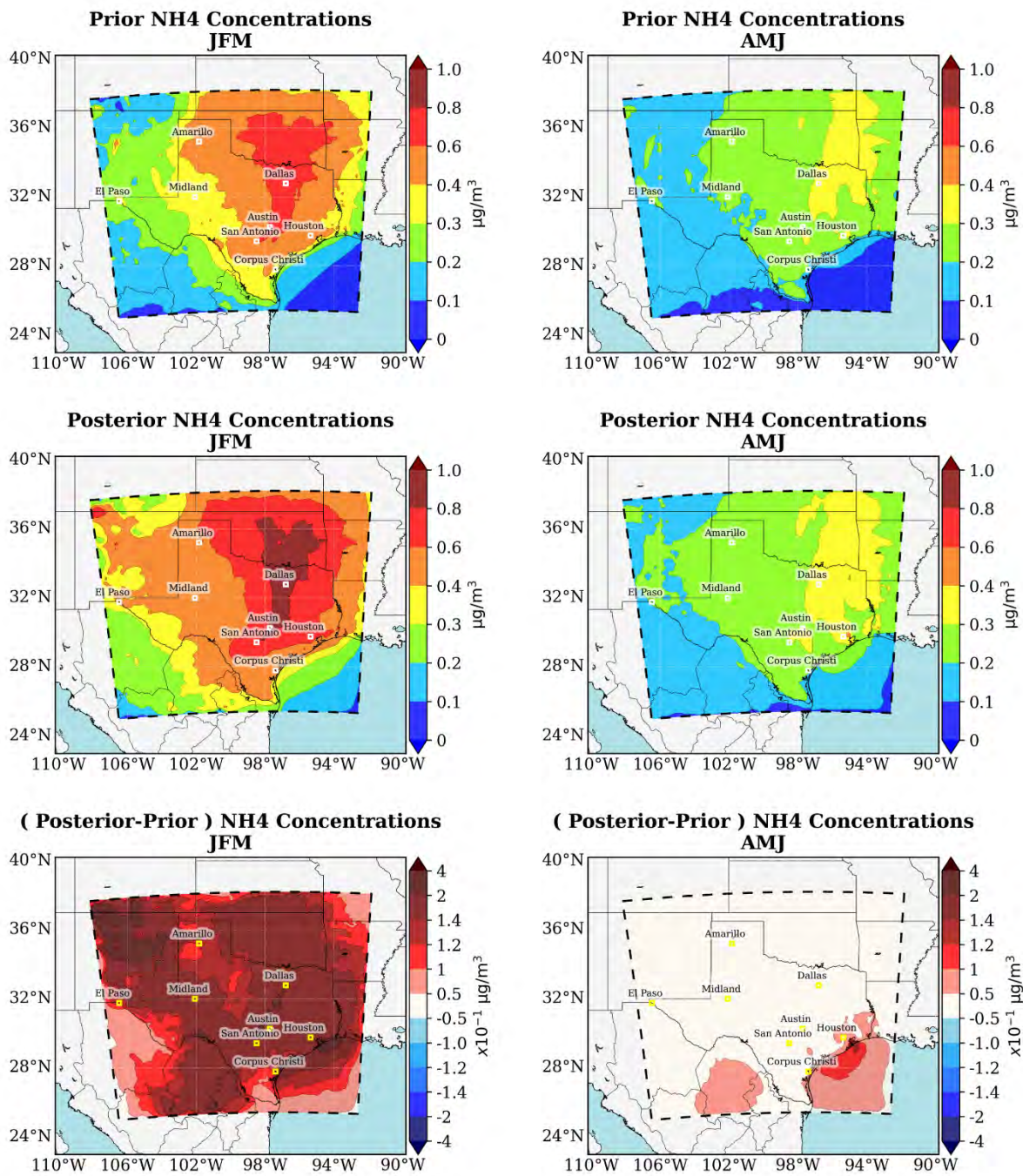
Figure 9 - continue
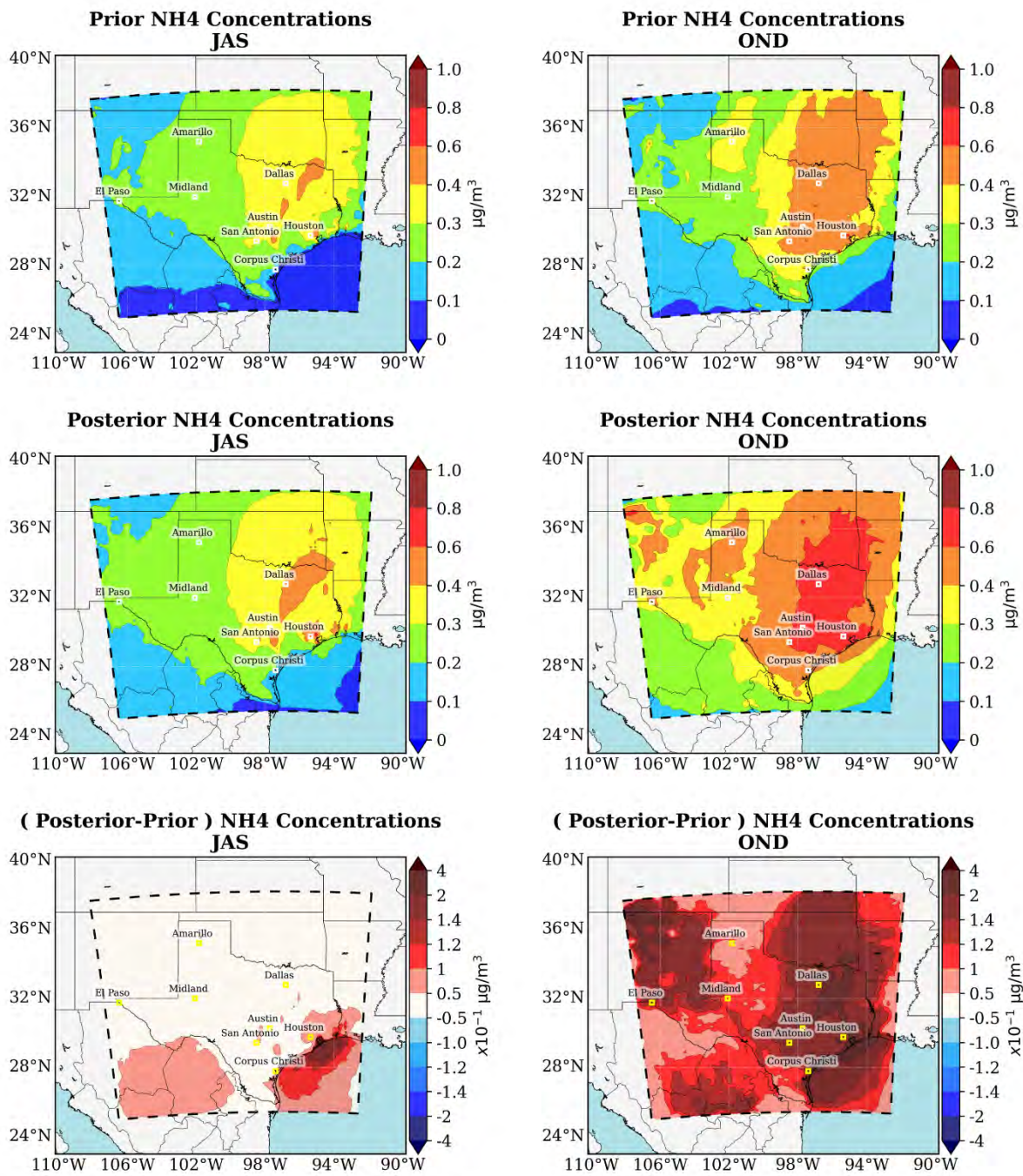
Figure 9 - continue
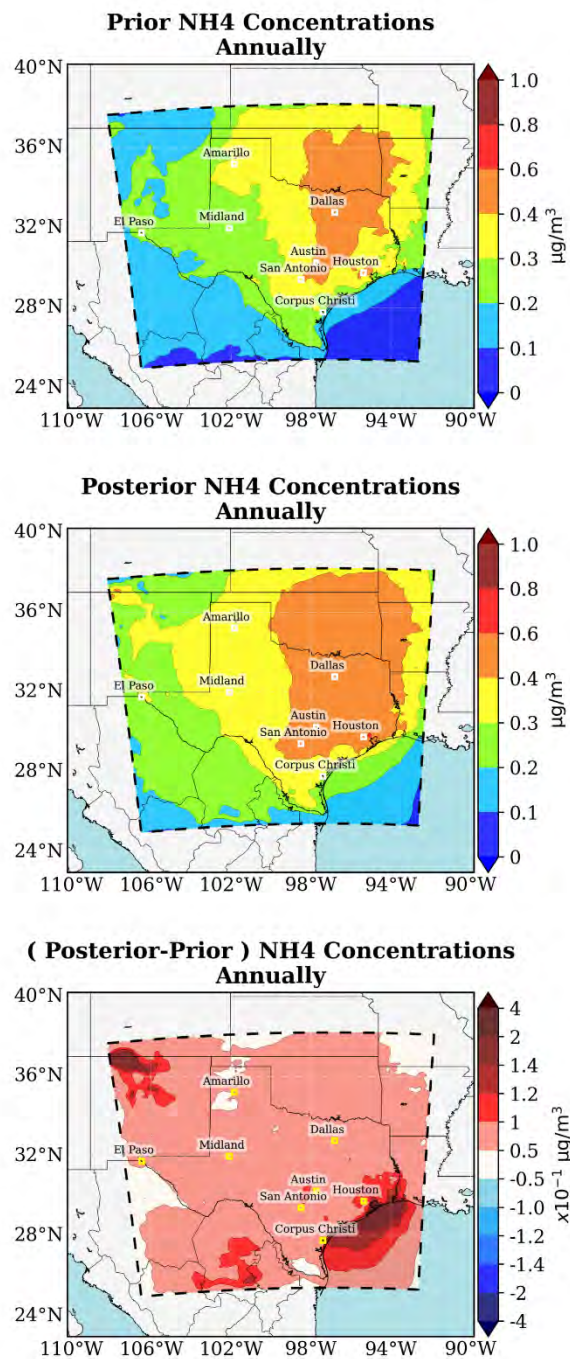
Figure 9: The spatial quarterly/annually averaged distribution for a-priori and a-posteriori NH_4^+ concentrations and their differences.

During JFM period, NH_4^+ concentrations have seen an increase across Texas, with relatively more modest increases observed in the Northwestern regions. Furthermore, heightened NH_4^+ values were simulated in the eastern parts of Texas, where the a-priori NH_4^+ concentrations were already higher compared to other areas. There was also a noticeable rise in NH_4^+ levels over the Gulf of Mexico, particularly along the shoreline. Specific hotspots of NH_4^+ near the Port Arthur and Galveston regions are noteworthy and warrant further investigation.

In contrast, the AMJ period, when IASI satellite wad used, did not witness any substantial changes in NH_4^+ levels over Texas. This can be attributed to the minimal increase in NH_3 concentrations during this period, which were not significant enough to cause a corresponding rise in NH_4^+. Since NH_3 and NH_4^+ are directly related ($NH_3 \rightleftharpoons NH_4^+$), a significant change in NH_3 typically corresponds to a change in NH_4^+. However, NH_4^+ concentrations did increase over the Gulf of Mexico, mirroring the trend seen in the JFM period. Notable hotspots near Arthur-port and Galveston were once again discernible, underscoring the importance of these regions in understanding sources of air pollutants.

During the JAS quarter, there wasn't a significant change in NH_4^+ concentrations across Texas, reflecting the similar stability in NH_3 values in the region. The observed NH_3 underestimation, in comparison with surface measurements (more detail in the evaluation section), could potentially be attributed to the lower values reported by the IASI satellite data used during the summer, resulting in lower a-posteriori NH_3 and NH_4^+ concentrations. Over the Gulf of Mexico, however, NH_4^+ displayed a significant increase, particularly in a prominent hotspot observed in the Southeastern parts near the Port Arthur and Galveston area. Notably, NH_4^+ values over the Gulf of Mexico increased more in the JAS quarter compared to the AMJ period.

In the OND quarter, NH_4^+ concentration patterns mirrored those seen in the JFM period. There was a significant increase in NH_4^+ values in the eastern parts of Texas, especially in areas with higher a-priori NH_4^+ concentrations. Over the Gulf of Mexico, NH_4^+ concentrations also rose, with a hotspot evident in the Southeastern part near the Port Arthur and Galveston area.

When considering an annual average, it was observed that NH_4^+ concentrations over Texas increased slightly, whereas values in the eastern part of the state increased more significantly. Over the Gulf of Mexico, NH_4^+ values escalated more compared to those over Texas. Furthermore, the notable hotspot over the Gulf of Mexico, particularly in the southern parts, warrants further investigation.

4.4.2. Sulfate concentrations

In the NH_3-HNO_3-H_2SO_4-H_2O system, sulfate initially tends to be neutralized by NH_3. Subsequently, if free NH_3 is present, it reacts with NO_3^- (Seinfeld & Pandis, 2016).

In JFM, SO_4^{2-} has increased over Texas, with more significant increases over the eastern part. As previously discussed, the higher NH_4^+ concentrations in the eastern part of the region have led to a more pronounced increase in SO_4^{2-} in these areas. This is attributed to the tendency of NH_4^+ to react with SO_4^{2-}, yielding ammonium sulfate $((NH_4)_2SO_4)$, both in solid and aqueous phases. Over the Gulf of Mexico, there has been an increase in SO_4^{2-} concentrations, which coincides with the same regions experiencing increased NH_4^+.

During the AMJ period, a-posterior SO_4^{2-} concentrations increased in the eastern part of Texas, a region characterized by both higher SO_4^{2-} a-priori values and a slight increase in NH_4^+. There were virtually no changes in SO_4^{2-} over the Gulf of Mexico, except in the southeastern shorelines. The observed hotspots near the Port Arthur and Galveston areas are particularly significant. In the JAS quarter, the alterations in SO_4^{2-} followed a pattern similar to that of AMJ. However, there were more increases in SO_4^{2-} at the identified hotspots.

In the OND period, there was a general rise in a-posterior SO_4^{2-} concentrations across Texas, with the eastern region experiencing more intense increases. Over the Gulf of Mexico, a similar trend in SO_4^{2-} increases were observed. Importantly, the majority of these SO_4^{2-} increases occurred in areas with high a-priori SO_4^{2-} concentrations, such as the Port Arthur and Galveston area. These locations are noteworthy due to the presence of industrial plants and shipping practices with high emission rates (Ge et al., 2021).
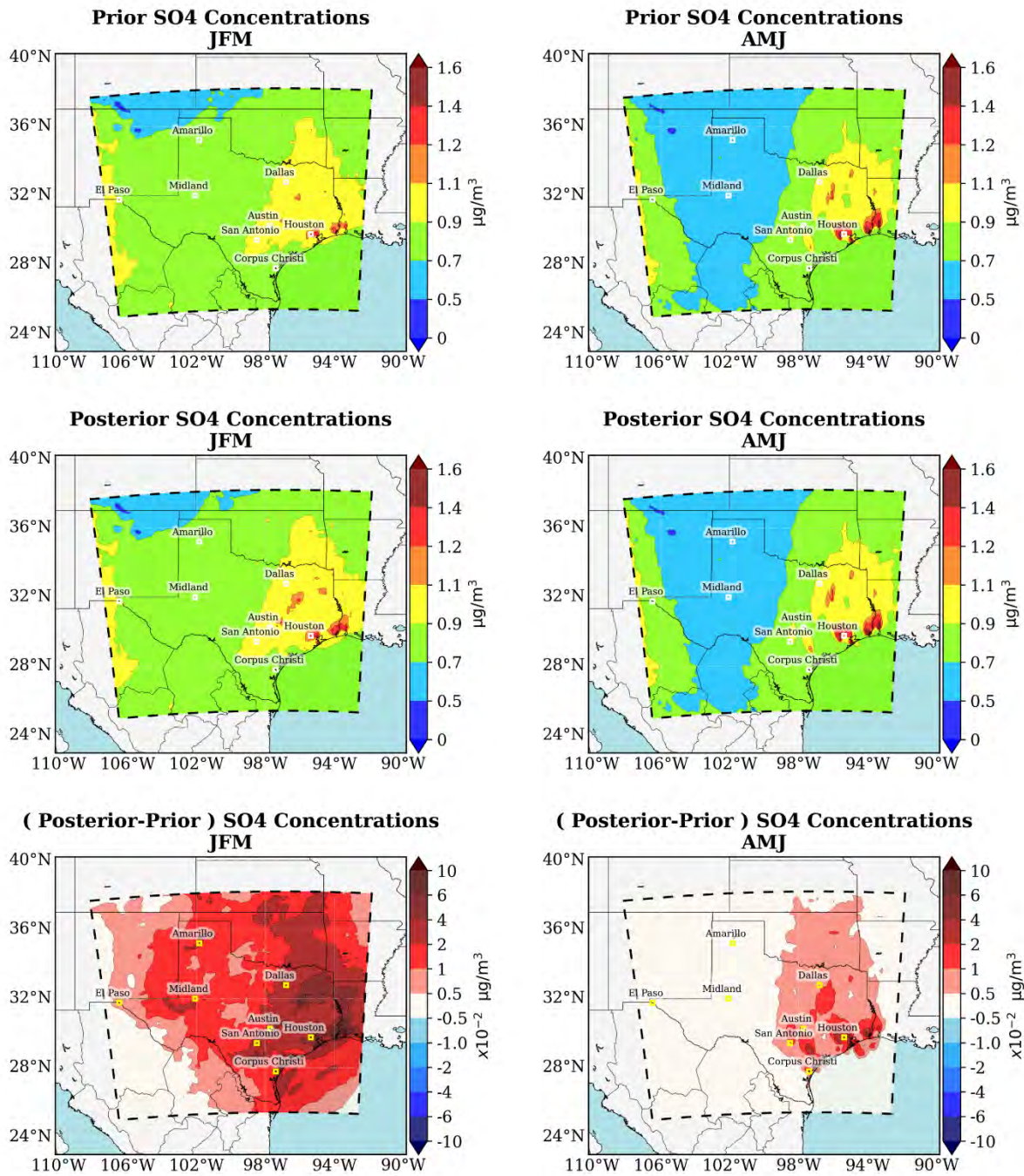
Figure 10 – continue
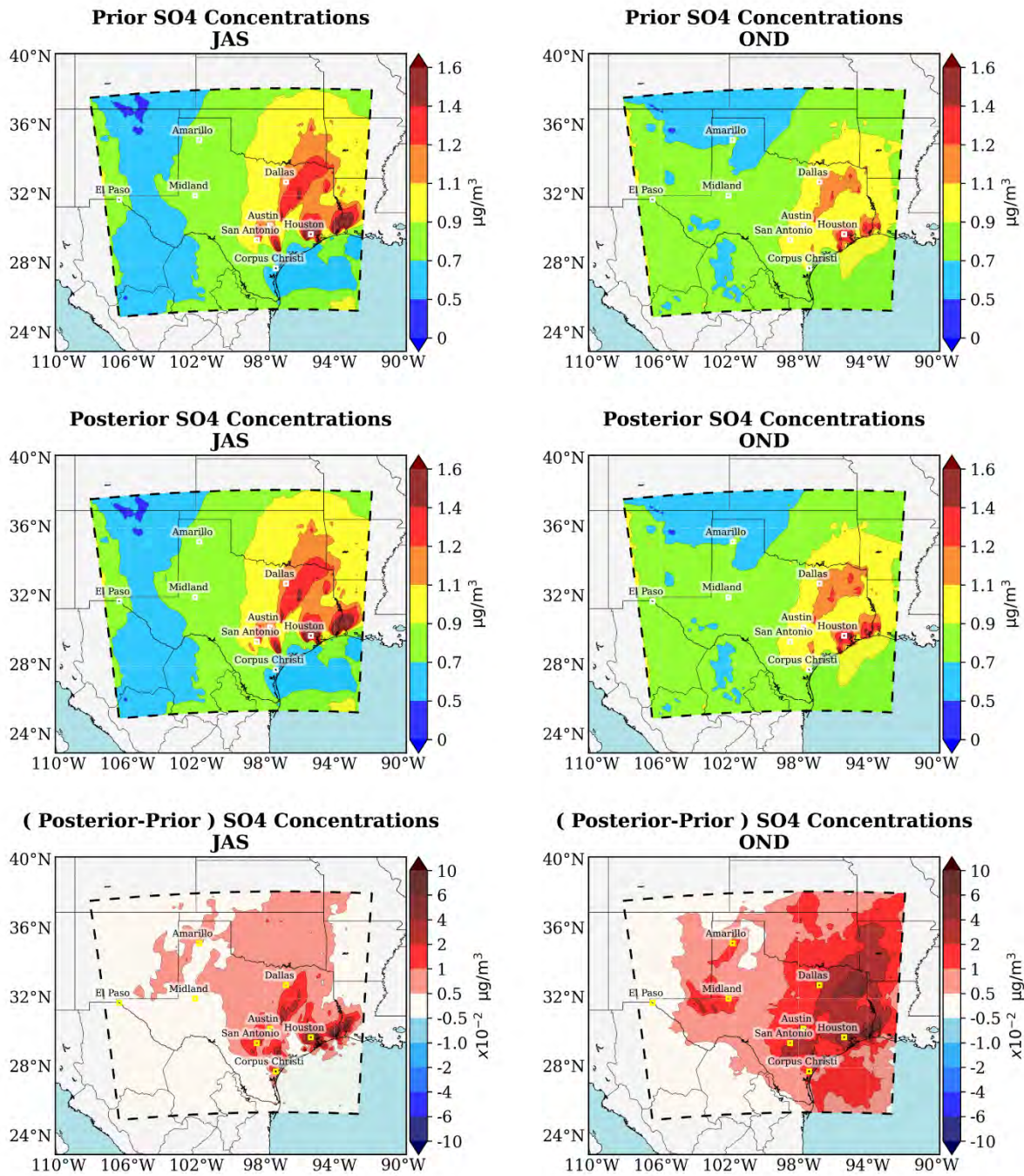
Figure 10 – continue
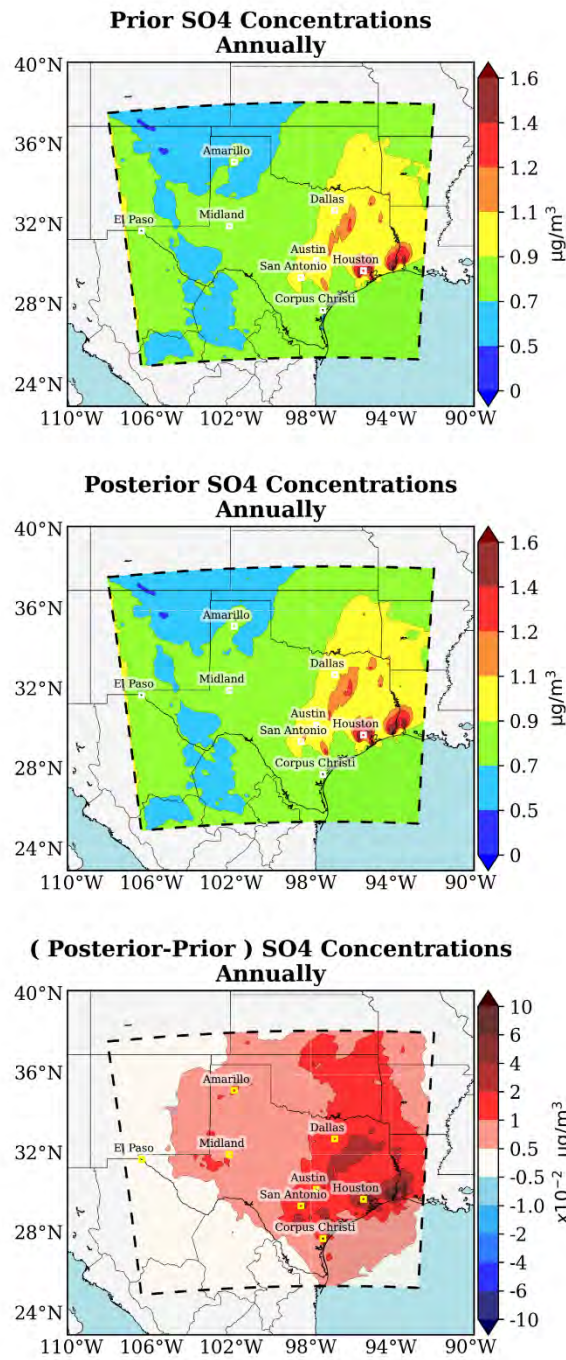
Figure 10: The spatial quarterly/annually averaged distribution for a-priori and a-posteriori SO_4^{2-} concentrations and its difference.

On the annual period, a-posteriori SO_4^{2-} concentrations experienced a greater increase in eastern Texas, particularly in areas where a-prior SO_4^{2-} concentrations were already high. Most notably, the significant increase in SO_4^{2-} concentrations near the Port Arthur and Galveston area, located in the southeast, emphasizes the potential importance of human activities, such as industrial operations and shipping, in contributing to the SO_4^{2-} emissions within this region.

4.4.3. Nitrate concentrations

Figure 11 shows the a-priori and a-posteriori NO_3^- concentrations and the difference between the a-posteriori and a-priori NO_3^- concentrations. For nitrate, if the regime is ammonia-poor in an NH_3-HNO_3-H_2SO_4-H_2O system, ammonium nitrate (NH_4NO_3) will be low or close to zero; if the regime is ammonia-rich, NH_3 reacts with NO_3^- when SO_4^{2-} is not present and neutralized by NH_3 (Seinfeld & Pandis, 2016).

In the JFM quarter, NO_3^- levels rose across Texas, particularly in regions that have high a-priori NO_3^- concentrations. It's crucial to note that an increase in NH_3 concentrations resulted from the increase in NH_3 emissions in this period led to an ammonia-rich regime across Texas. In such conditions, NO_3^- levels are likely to rise, as sufficient adequate NH_3 is present to neutralize SO_4^{2-}, and excess NH_3 contributes to increased NO_3^- production. Moreover, significant increases in NO_3^- levels were noted over the Gulf of Mexico.

During both the AMJ and JAS quarters, no significant increases were seen in a-posteriori NO_3^- concentrations over Texas, likely due to a-posteriori NH_3 concentrations not being high enough to neutralize SO_4^{2-}. It is, however, important to highlight the observed increases in a-posteriori NO_3^- concentrations over the Gulf of Mexico near the Port Arthur and Galveston area during these periods.

In OND, the patterns are similar to those of JFM. The increase in a-posteriori NH_3 levels led to an ammonia-rich system over Texas, and increases in NO_3^- levels resulted due to sufficient NH_3 to neutralize SO_4^{2-}, with the remainder of the ammonia contributing to NO_3^- production. Furthermore, marked increases in NO_3^- levels were also simulated over the Gulf of Mexico in this period.
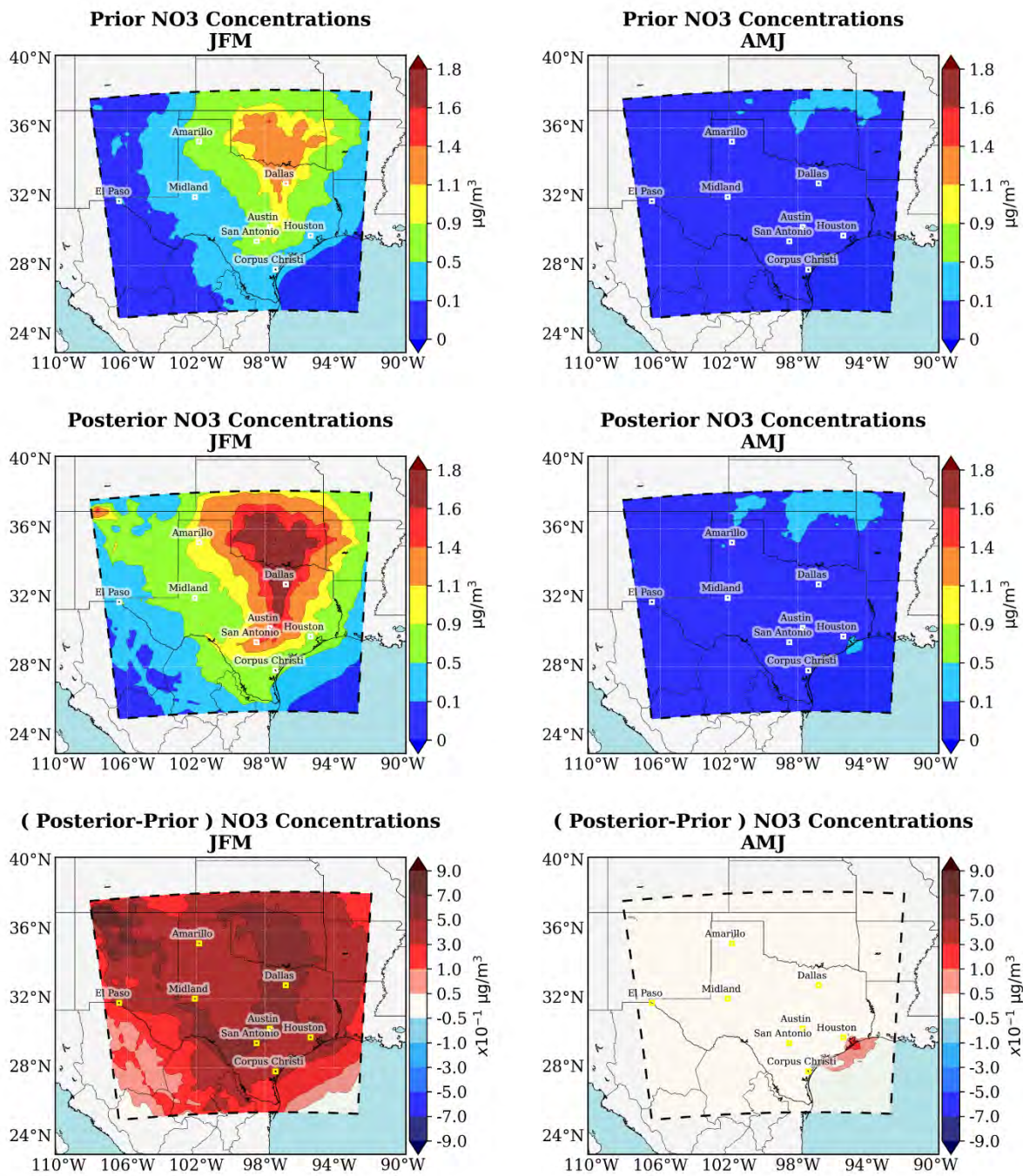
Figure 11 – continue
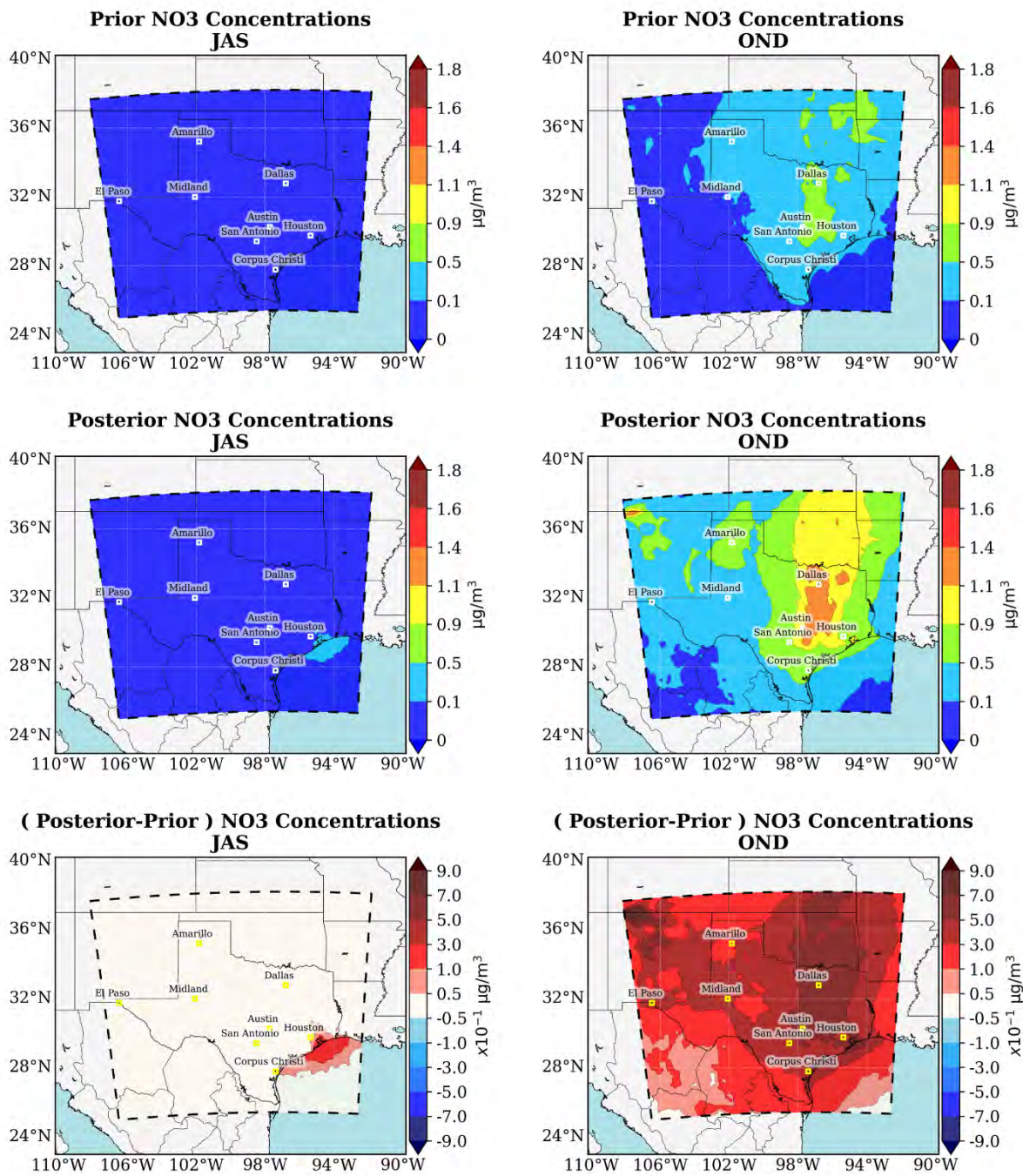
Figure 11 – continue
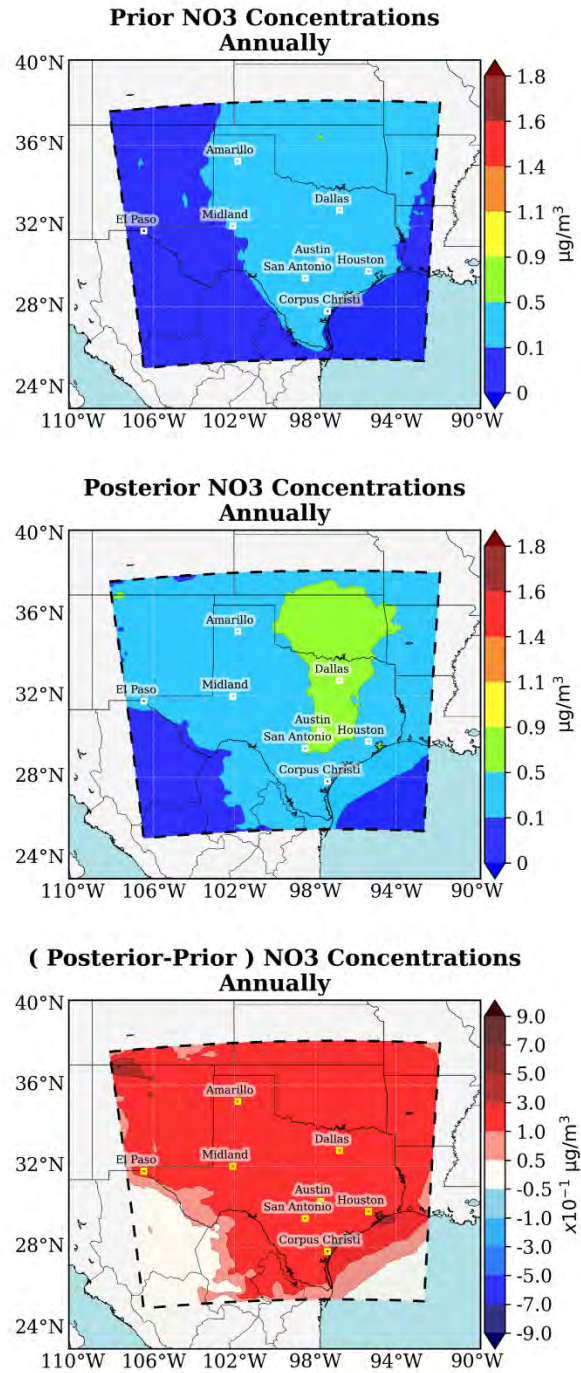
Figure 11: The spatial quarterly/annually averaged distribution for a-priori and a-posteriori NO_3^- concentrations and their differences.

When considering the annual averages for NO_3^-, increases were simulated throughout Texas. The elevated NH_3 has likely resulted in an ammonia-rich regime where adequate NH_3 neutralizes SO_4^- to form NO_3^- production. The enhanced a-posteriori NO_3^- levels along the shoreline in the Gulf of

44

Mexico are also noteworthy. This increase may be attributable to the high levels of SO_2 stemming from shipping activities, further emphasizing the human influence on these emissions.

4.5. Evaluation

4.5.1. RCCM

For this project, NH_3 concentrations simulated by the RCCM were evaluated by the standard CMAQ model to make sure that the RCCM model produces reasonable results. In Figure 12, the comparison of NH_3 , NH_4^+, SO_4^{2-}, and NO_3^- in Aitken mode with subscript I and accumulation mode with subscript J modes simulated by the RCCM and those by the standard model are shown. The results illustrate that the RCCM was in closer agreement with the standard CMAQ.

4.5.2. Posterior evaluation with satellite observations

Figure 13 displays the spatial distribution of satellite, a-priori, and a-posteriori NH_3 column density on a quarterly and annual basis, including the differences among them. The figure reveals that the iFDMB was successful in capturing the spatial pattern of the NH_3 column density as per CrIS and IASI data. However, in the northern part of the domain, the iFDMB seems to slightly overestimate, while in the southwest region, it tends to underestimate. This is likely due to the iFDMB's limitations in adjusting low-value data.

Figure 14 shows the scatter plot for the column density of ammonia over Texas, including all data points from the model. Table 4 displays a comparative Evaluation of Model Performance Metrics against satellite column density for prior/posterior NH_3 column density versus satellite across different quarters and annually.

In JFM the model was not performing well in the prior evaluation, with a near-zero correlation coefficient and the highest error metrics among all quarters. However, after the update (posterior), the performance significantly improved across all metrics. The correlation coefficient (R) increased to 0.83, suggesting a much stronger positive relationship between predicted and observed values. The error metrics (MAE, NMSE, RMSE) have all decreased, indicating that the predictions are more accurate, and the IOA increased to 0.91, showing a high degree of agreement between the predicted and actual values.
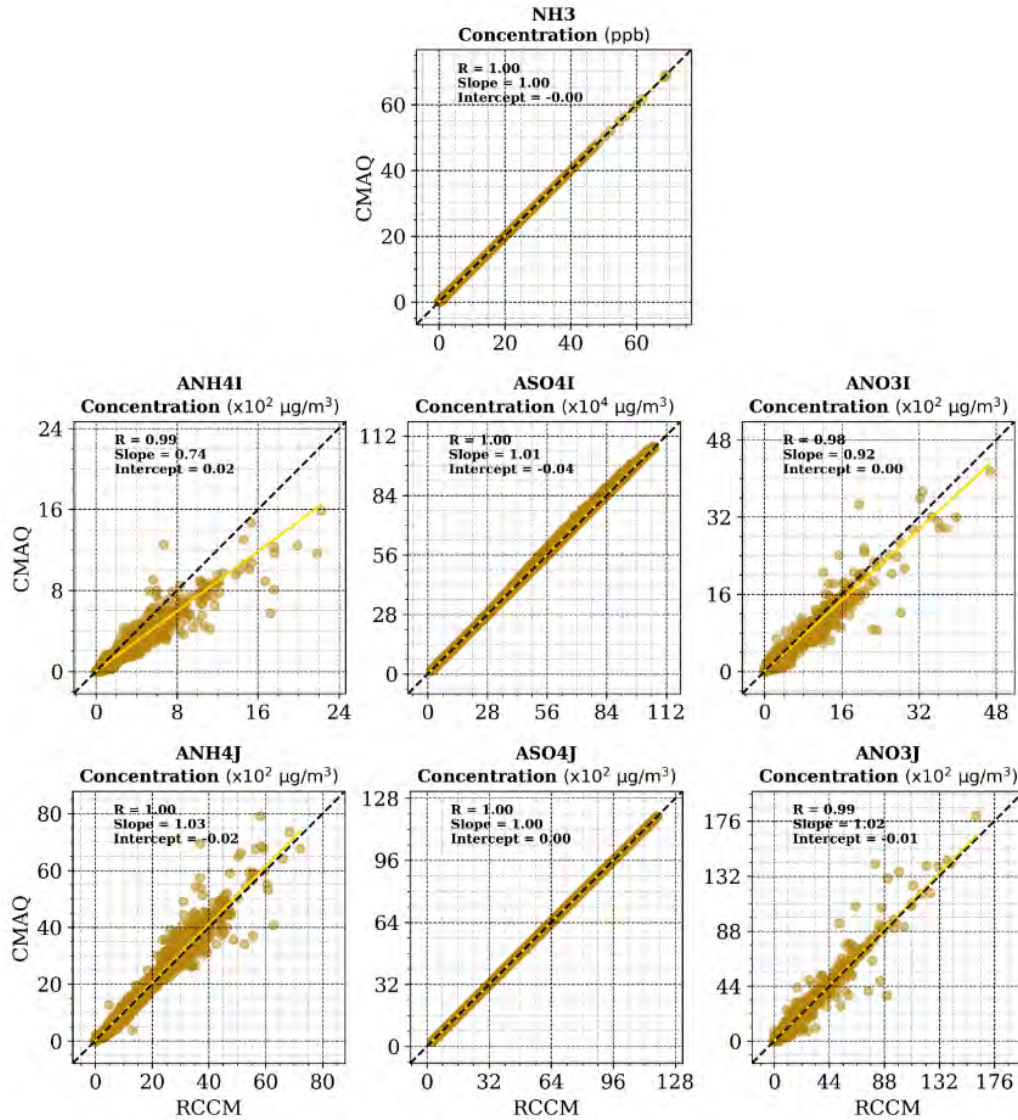
Figure 12: Comparison of the standard CMAQ predictions with RCCM predictions for NH_3, NH_4^+, SO_4^{2-}, and NO_3^-.

In AMJ, the model performance in this quarter also improved substantially. The correlation coefficient increased from 0.47 to 0.87, showing a strong positive linear relationship in the posterior model. The error metrics all decreased, again suggesting improved accuracy, and the IOA increased from 0.39 to 0.92, showing an almost perfect agreement.

In JAS, significant improvements in all metrics were observed. The correlation coefficient increased from 0.52 to 0.91 while all the error metrics decreased. The IOA value reached 0.95, suggesting an almost impeccable match between the predicted and the actual values.
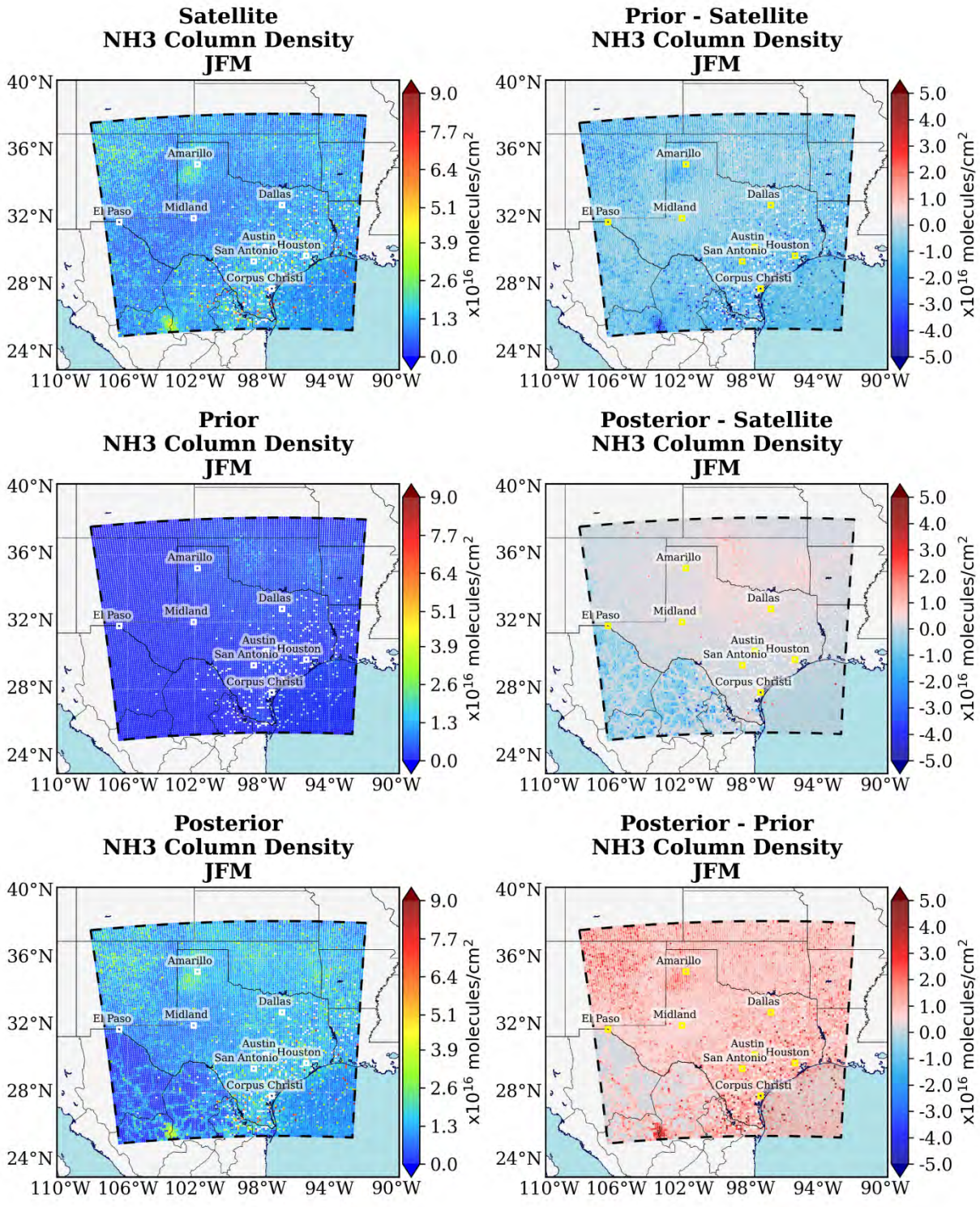
Figure 13 - continue
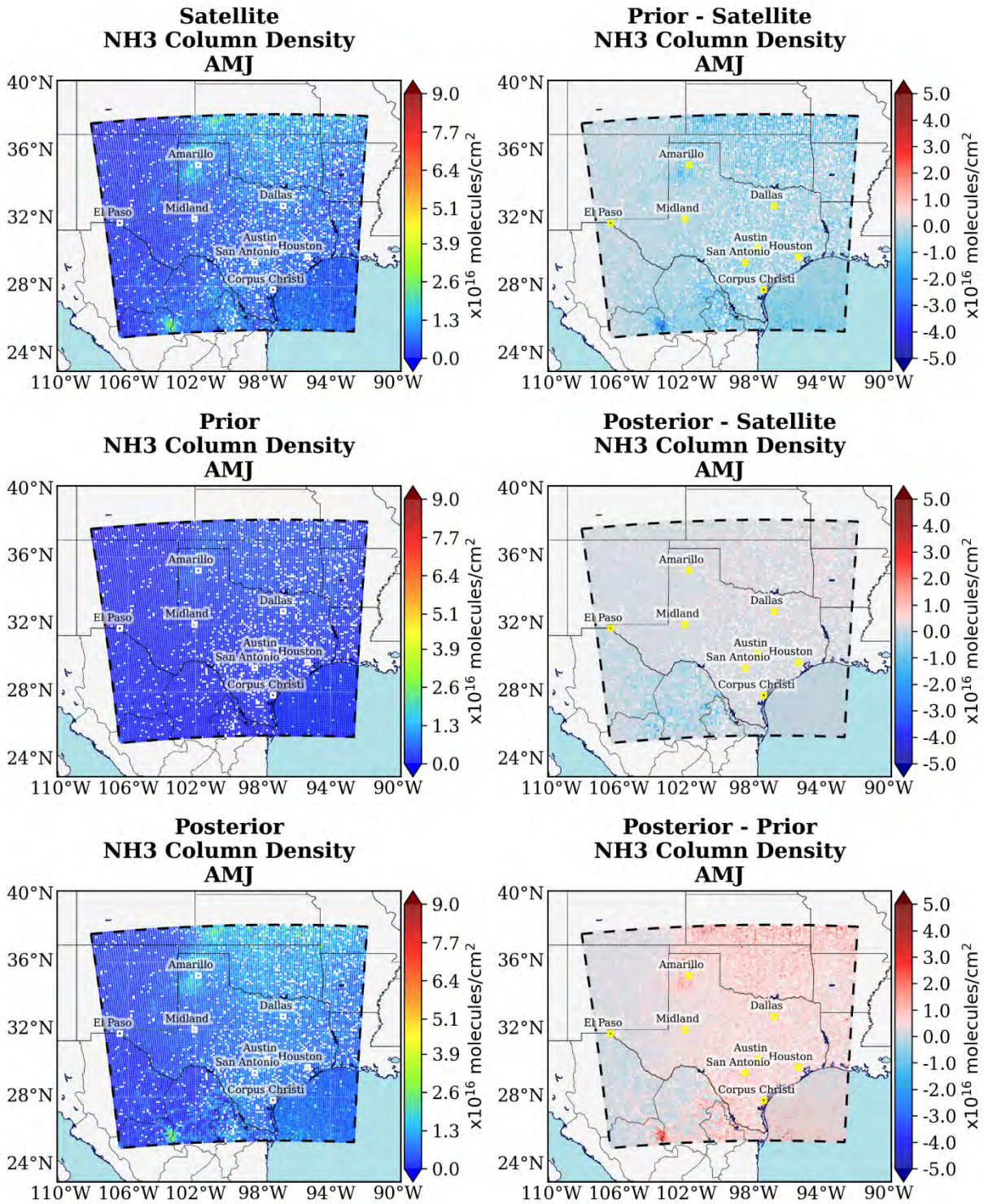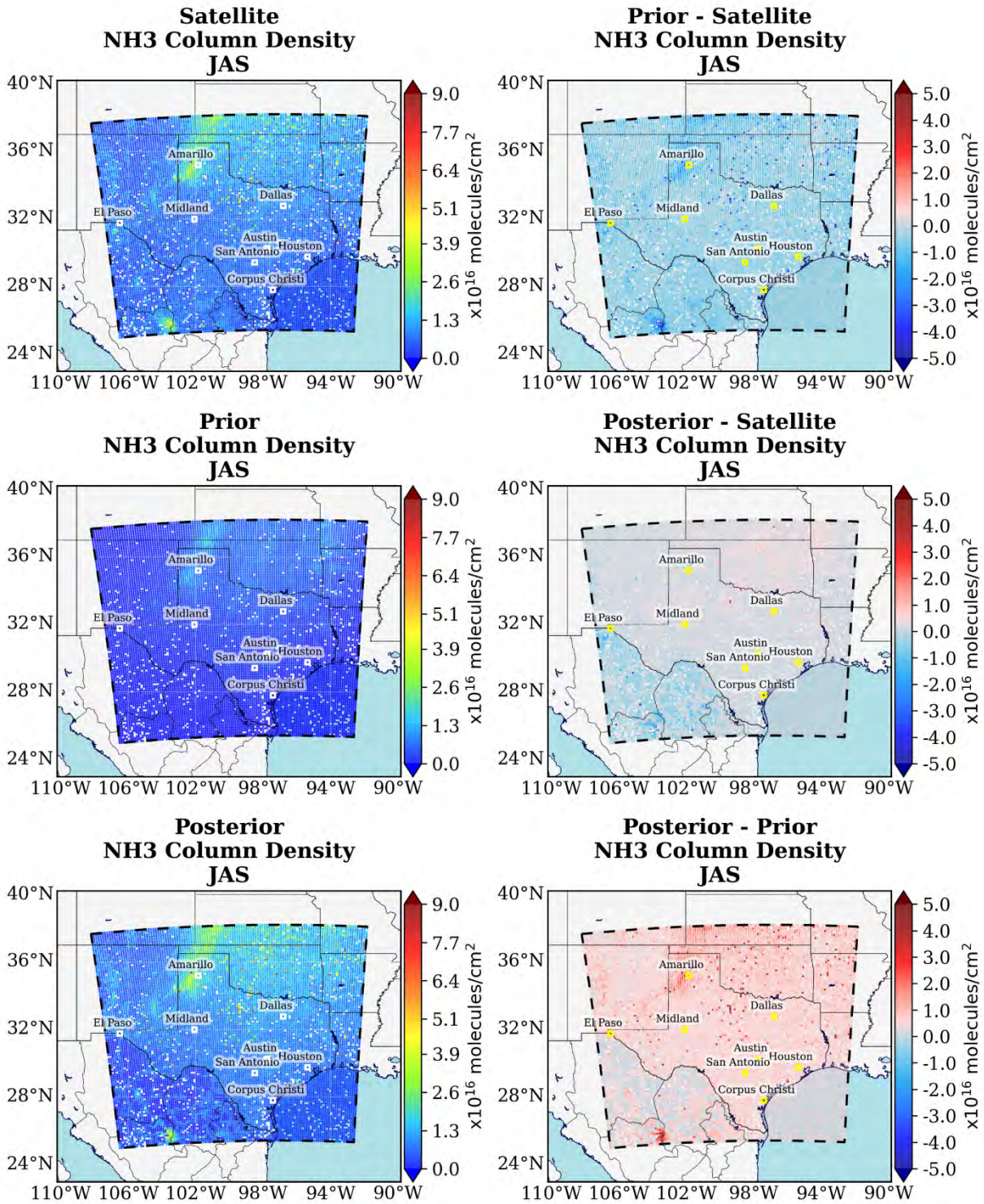
Figure 13 - continue
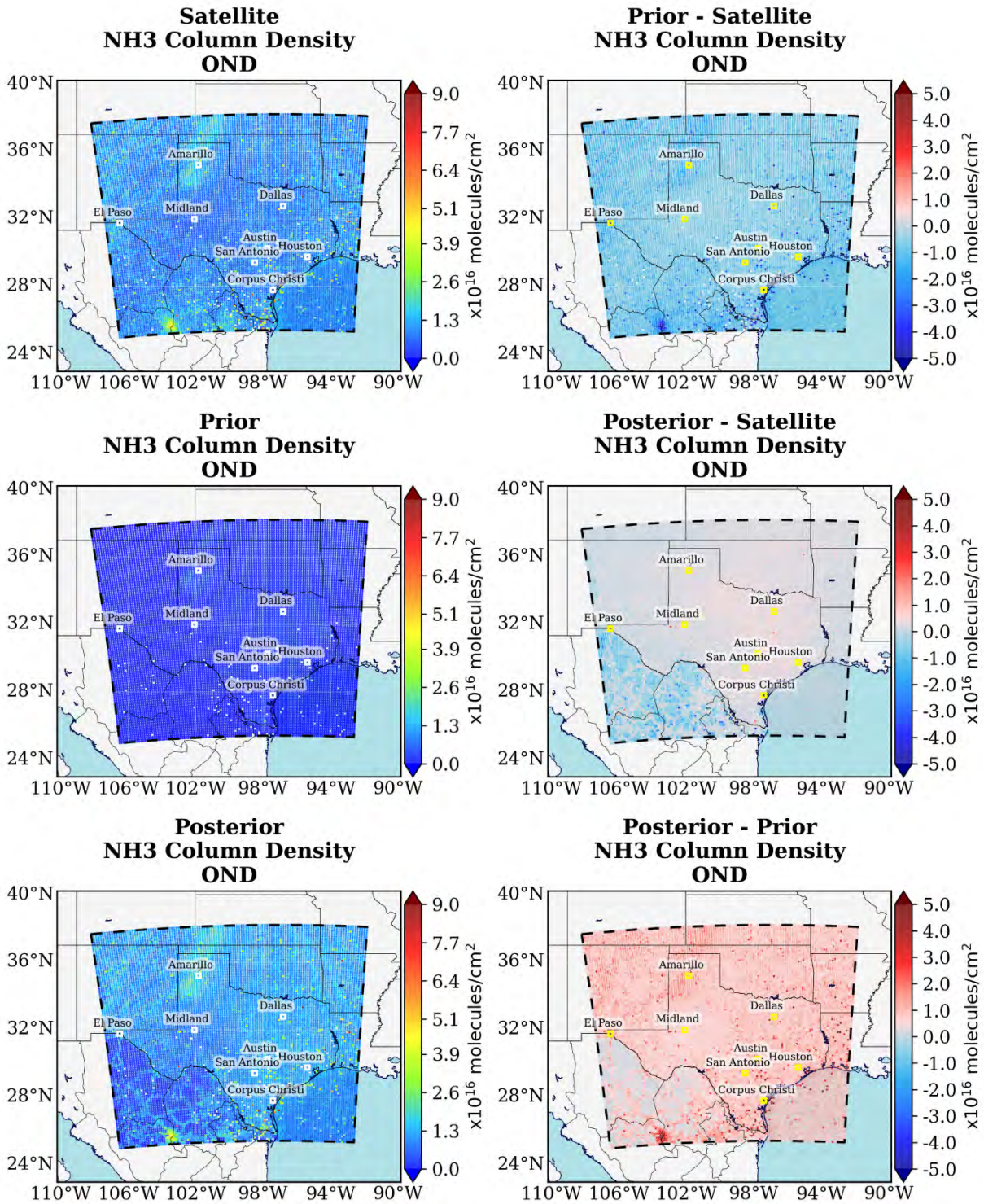
Figure 13 - continue

Figure 13 - continue
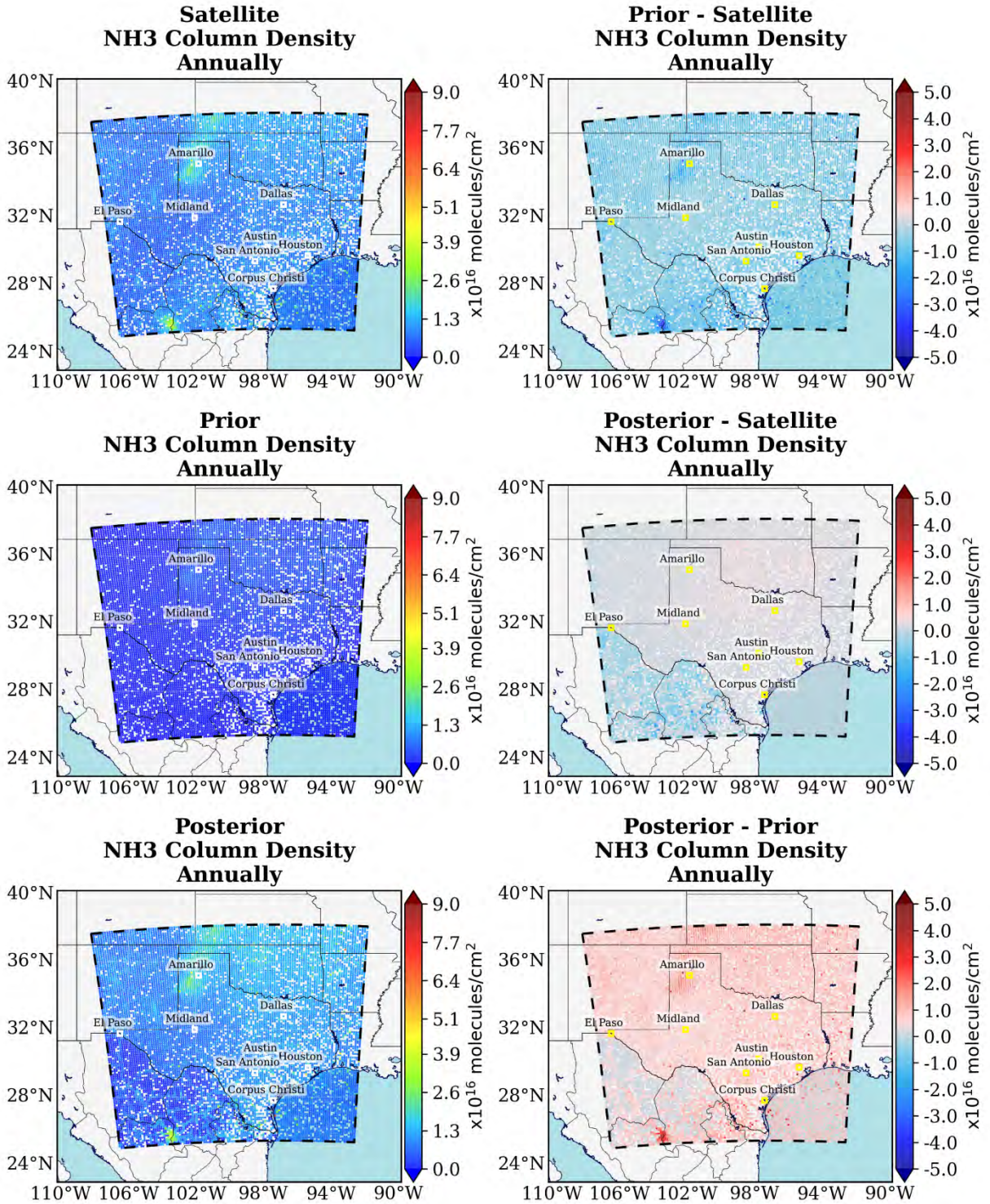
Figure 13: The spatial quarterly/annually averaged distribution for satellite, a-priori, a-posteriori, and their differences for NH_3 column density.
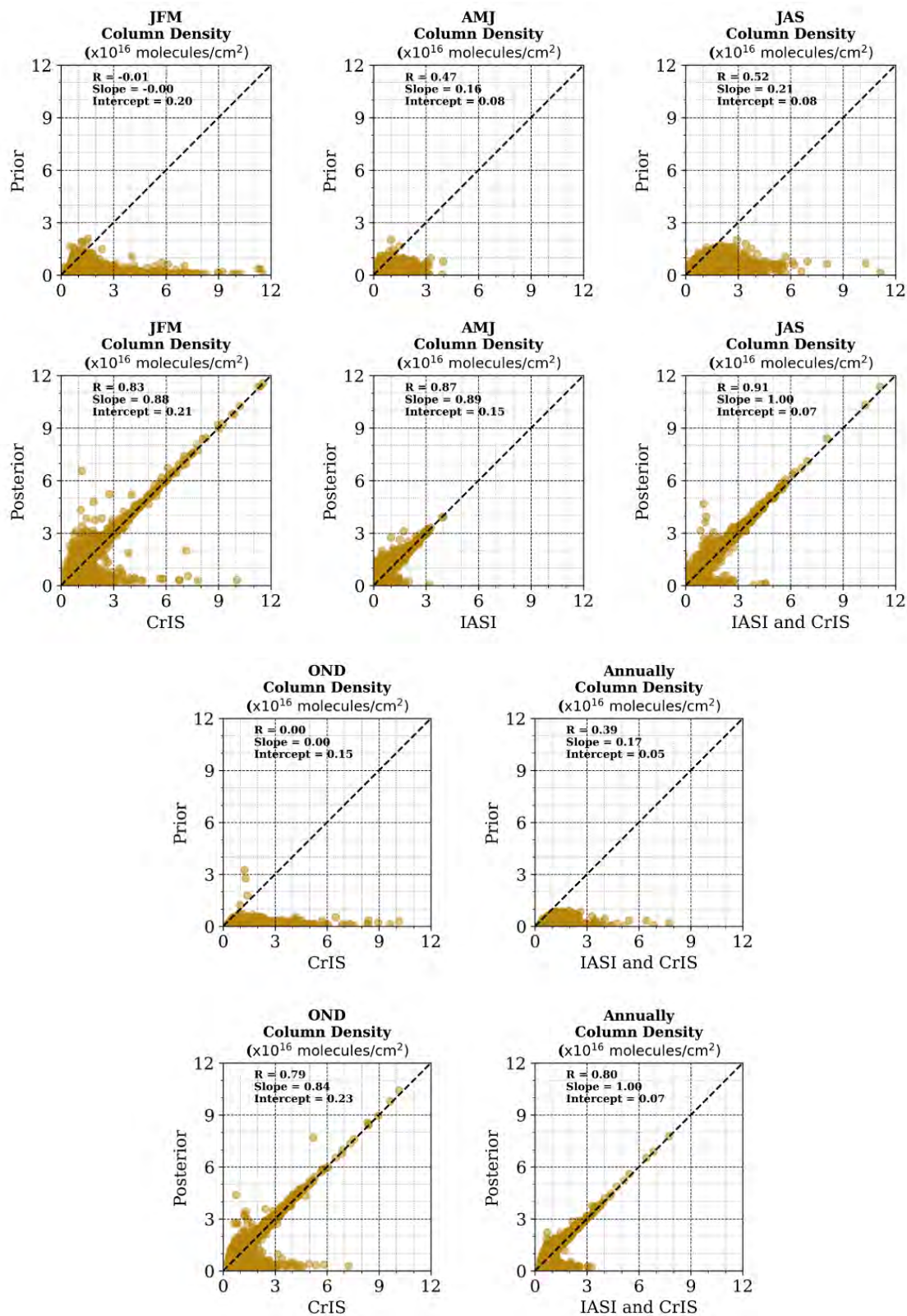
Figure 14: Scatter plot for the NH_3 column density for the comparison between a-priori and a-posteriori results versus AMoN

Table 4: Comparative Evaluation of Model Performance Metrics against satellites data (IASI and CrIS) for NH_3 column density (Errors unit is molecules/cm$^2 \times 10^{-16)}$

Quarter		R	MAE	NMSE	RMSE	IOA
JFM	Prior	-0.01	1	6.82	1.26	0.65
	Posterior	0.83	0.27	0.13	0.45	0.91
AMJ	Prior	0.47	0.42	2.99	0.55	0.39
	Posterior	0.87	0.17	0.15	0.24	0.92
JAS	Prior	0.52	0.59	2.95	0.80	0.48
	Posterior	0.91	0.19	0.10	0.28	0.95
OND	Prior	0.0002	0.88	6.95	1.04	0.67
	Posterior	0.79	0.23	0.12	0.36	0.89
Annually	Prior	0.39	0.70	3.32	0.77	0.39
	Posterior	0.80	0.20	0.09	0.28	0.89

In OND, this quarter indicated the most dramatic improvement in terms of the correlation coefficient, which increased from near zero to 0.79. The error metrics were all reduced significantly, and the IOA value rose from 0.67 to 0.89, indicating a strong agreement between predicted and actual values.

In annual values, Like the quarterly results, the annual results also improved in every metric. The correlation coefficient rose from 0.39 to 0.80, showing a stronger positive linear relationship. The error metrics all decreased, indicating better overall prediction accuracy, and the IOA rose from 0.39 to 0.89, showing a strong overall agreement between predicted and actual values.

In conclusion, the posterior simulation performs substantially better than the prior simulation across all quarters and on an annual basis in terms of all the measured metrics.

4.5.3. Posterior evaluation with surface measurements

Figure 15 shows a comparison of the AMoN (surface measurements), priori, and posterior concentrations for NH_3. For the months of August, May, and June (AMJ), the concentration was updated to more than 50% of the initial model value, while the posterior still underestimates the observation. In the months of July, August, and September (JAS), the posterior is updated and increased to about 1.8 µg/m³, yet it still shows underestimation compared to the observation. In the months of January, February, and March (JFM), very low amounts of ammonia are observed, while the priori is about two times lower. The posterior for JFM captures the underestimation of

the priori and updates the ammonia concentration to about 1.9 µg/m³. For October, November, and December (OND), the posterior overestimates the ammonia concentration by the value of 2.3 µg/m³, whereas the AMoN shows a value of about 1.5 µg/m³.

Table 5 and Figure 16 show a comparison of performance metrics between a priori and a posteriori concentrations against the AMoN concentrations for NH_3. The results display that the correlation coefficient (R) has slightly improved from 0.49 to 0.52. This indicates a small but positive improvement in the linear relationship between the predicted and observed values.

All the error metrics, including Mean Absolute Error (MAE), Normalized Mean Squared Error (NMSE), and Root Mean Squared Error (RMSE), have decreased in the posterior simulation. MAE reduced from 1.17 to 0.92, NMSE fell significantly from 1.46 to 0.38, and RMSE decreased from 1.67 to 1.20. These decreases imply that the updated NH_3 emissions have improved simulation accuracy compared to the a-priori emissions.

The Index of Agreement (IOA) increased from 0.54 to 0.67 in the posterior simulation, suggesting a better agreement between the simulated and observed values in the updated emissions compared to the a-priori emissions. Overall, the table shows that the updated (posterior) NH_3 emissions provide an overall improved performance over the prior NH_3 emissions, offering more accurate predictions and a better fit with observed values.
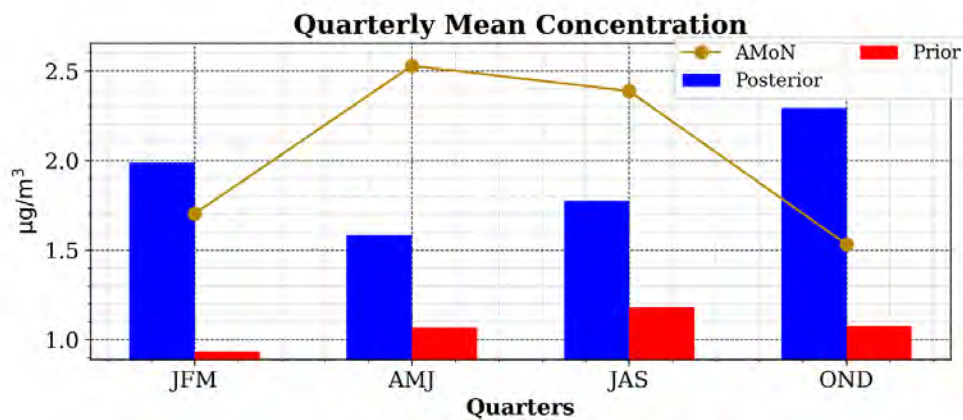
Figure 15: The comparison of AMoN, priori, and posterior of NH_3 concentrations.

Table 5: Performance metrics between a prior and a posterior biweekly averaged NH_3 concentrations against AMoN (Errors unit: µg/m³).

	R	MAE	NMSE	RMSE	IOA
Prior	0.50	1.17	1.46	1.67	0.54
Posterior	0.52	0.92	0.38	1.20	0.67
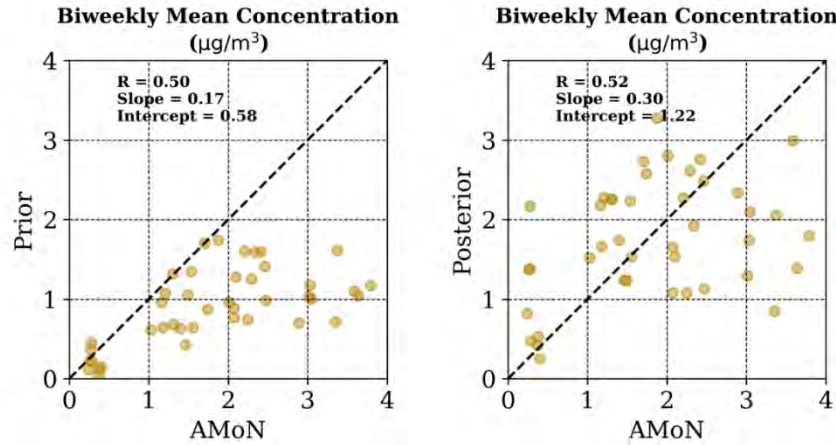
Figure 16: Scatter plot for the NH_3 concentration for the comparison between biweekly averaged a-priori and a-posteriori results versus AMoN.

Figure 17 shows a monthly comparison of the NTN, priori, and posterior wet deposition for NH_4^+. Across all months, the updated emissions enhanced the values for NH_4^+ wet deposition, especially in June and August, compared to the NTN. However, wet deposition remains underestimated for other months. It's noteworthy that wet deposition data was unavailable for January and February.
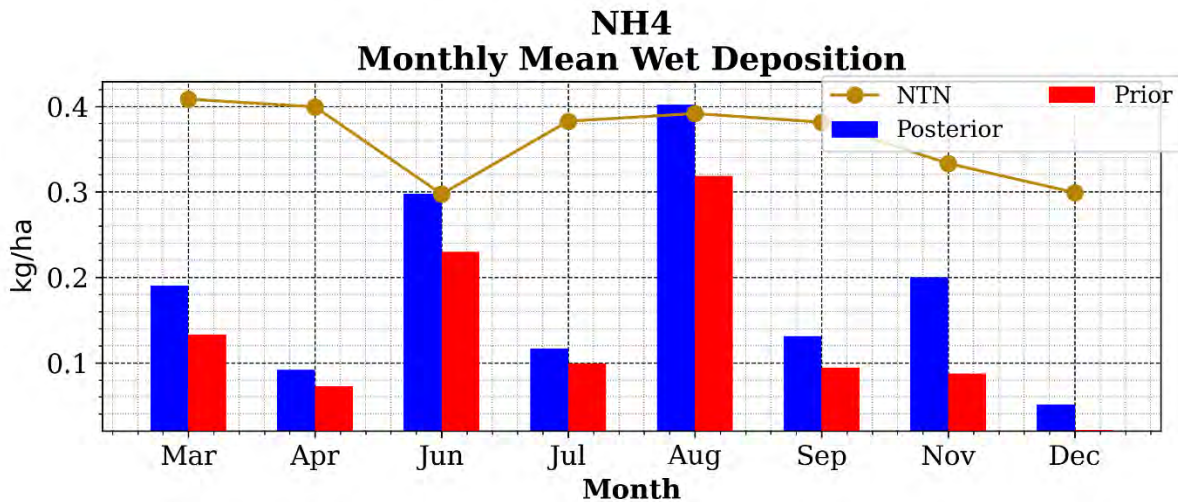
Figure 17: The comparison of NTN, priori, and posterior of NH_4^+ wet deposotions.

Table 6: Performance metrics between a prior and a posterior weekly averaged NH_4^+ wet deposition against NTN (Errors unit: kg/ha).

	MAE	NMSE	RMSE	IOA
Prior	0.28	2.58	0.34	0.40
Posterior	0.26	1.71	0.33	0.37

Table 6 compares the performance metrics of a model both prior and posterior wet deposition versus the NTN. There's a slight improvement in the MAE value post-wet deposition, decreasing from 0.28 to 0.26. This suggests that, on average, the model's simulations are now slightly closer to the observed values. The NMSE sees a significant reduction from 2.58 in the prior evaluation to 1.71 in the posterior evaluation, indicating a marked improvement in the model's accuracy. The RMSE value has a marginal reduction from 0.34 to 0.33, suggesting a modest improvement in the model's performance. The IOA sees a decrease from 0.40 to 0.37. This decrease suggests that the model's predictions are slightly less in agreement with observations in the posterior evaluation compared to the prior. In general, the posterior result seems to have improved the MAE, NMSE, and RMSE values, but the IOA has decreased slightly.

In Figure 18, the box plot illustrates the difference between a-priori and a-posteriori NH_4^+ wet deposition values when compared with the NTN. The results highlight an improvement in the a-posteriori NH_4^+ wet deposition, though it remains underestimated.
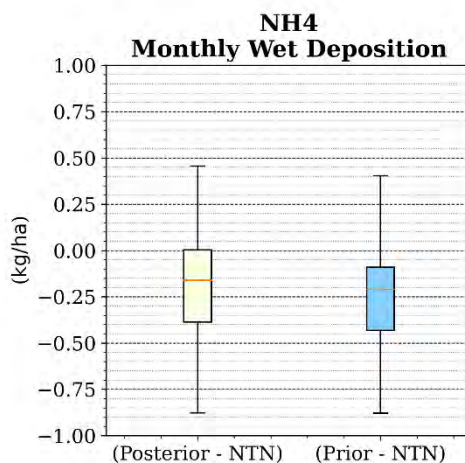
Figure 18: Box plot for the comparison between the difference of a-priori and a-posteriori NH_4^+ wet deposition with NTN.

5. Conclusions and recommendations

In conclusion, this study successfully implemented an inverse modeling technique using satellite data to improve NH_3 emissions over Texas and the Gulf of Mexico. National Emissions Inventory (NEI) 2017 was used to produce NH_3 emissions from mobile, area, and point sources, including anthropogenic and biogenic sources, in 2019. For oceanic biogenic NH_3 emissions, while the NEI does not account for Biological Nitrogen Fixation, EDGAR was employed to quantify these emissions for the Gulf of Mexico region. The iterative Finite Difference Mass Balance (iFDMB) method effectively incorporated CrIS and IASI satellite observations to constrain and revise the NEI NH_3 emissions inventory for 2019. A data gap from March 25 to August 12 2019, resulting from the unavailability of CrIS observations, presented complications in relying solely on CrIS satellite data for annual NH_3 emissions adjustments. To address this, IASI observational data is integrated to compensate for the absent information for 2019. Since running iFDMB is computationally expensive and requires numerous iterations, to reduce the burden of computations while maintaining the accuracy of predictions, we developed a Reduced Complexity CMAQ Model (RCCM), and the results showed that it was capable of replacing standard CMAQ with very little bias. To assess the efficiency of the model and posterior emissions, an evaluation was made between the posterior and prior estimates versus data from the CrIS/IASI satellites and surface measurements. For the surface measurements, the Ammonia Monitoring Network (AMoN) for NH_3 concentrations and the NADP's National Trends Network (NTN) for NH_4^+ wet depositions were employed. In the end, changes in concentrations of NH_3 and inorganic $PM_{2.5}$ species such as ammonium (NH_4^+), sulfate (SO_4^{2-}), and nitrate (NO_3^-) were explored after adjusting the NH_3 emissions inventory.

The findings revealed that annual NH_3 emissions in Northwestern Texas exhibited an increase exceeding 100 tons, while in the Southeastern sectors, the enhancement surpassed 50 tons. In several Texas regions where previous emission metrics registered zero, increments between 10 and 50 tons were discerned. Significantly, over the Gulf of Mexico, emissions transitioned from a null baseline to values exceeding 50 tons, emphasizing the prevailing uncertainties in oceanic biogenic NH₃ emission estimations.

Analyzing annual average NH_3 concentrations, a clear increase in NH_3 levels throughout Texas is obtained. The most significant increase, a rise of 3-4 ppb, is evident in the Northwestern regions. Conversely, most northern and certain eastern parts of Texas show a modest increase, hovering around 1-2 ppb. This 1-2 ppb elevation over the Gulf of Mexico emphasizes the pivotal role of marine sources, likely driven by biological nitrogen fixation and activities linked to the maritime and oil sectors.

Upon annual analysis, NH_4^+ concentrations in Texas exhibited a modest increase, with a more marked rise in the eastern regions. Over the Gulf of Mexico, these concentrations amplified further, particularly in the southern zone, meriting further scientific investigation. SO_4^{2-} levels in eastern Texas, especially in areas with already high concentrations, showed a notable rise. The marked increase near Port Arthur and Galveston in the southeast suggests a significant impact from human activities like industry and shipping. For NO_3^-, a rise was observed across Texas. The increased NH_3 might have led to an ammonia-rich regime where adequate NH_3 neutralizes SO_4^{2-}, forming NO_3^- production. Notably, the increased NO_3^- concentrations along the Gulf's shoreline could be linked to high SO_2 levels from shipping, highlighting the human impact on these emissions.

For the evaluation, compared to the CrIS/IASI satellites, The posterior simulation consistently outperformed the prior simulation across each quarter and annually for all evaluated metrics. Compared to AMoN, the posterior NH_3 emissions provide an overall improved performance over the prior NH_3 emissions, offering more accurate predictions and a better fit with observed values. When contrasted with NTN, the posterior result seems to have improved the statistical metrics.

Key outcomes include:
- Development of a Reduced Complexity CMAQ Model (RCCM) that maintained accuracy while reducing computational burden.
- Application of the iFDMB technique increased NH_3 emissions compared to prior NEI estimates, reflecting high uncertainty in NEI NH_3 emissions inventory, particularly over the Gulf of Mexico.
- Annual NH_3 emissions increased by over 100 tons in Northwestern Texas and over 50 tons in Southeastern regions.

- NH_3 concentrations rose across Texas, increasing 3-4 ppb in the Northwest and 1-2 ppb elsewhere.
- NH_3 emissions and concentration levels notably increased over the Gulf of Mexico, indicating underestimated ocean sources.
- Higher ammonium, sulfate, and nitrate concentrations were simulated in Eastern Texas using updated NH_3 emissions.

Future work should focus on multi-year emission constraints, advanced data assimilation techniques, improved calibration of satellite data, and identification of source contributions to elevated NH_3 levels in Southeastern Texas and particularly over the Gulf of Mexico. Inverse modeling with satellites shows strong potential for addressing uncertainties in bottom-up emission inventories.

6. Audits of data Quality

We performed Quality Assurance/Quality Control (QA/QC) procedures in accordance with the Quality Assurance Project Plan (QAPP) completed at the beginning of this project. Per requirements for Category III projects, we performed data audits on at least 10% of the data sets. In this section, we report the results of our QA/QC.

APPENDIX: Evaluation metrics

To evaluate the performance of CMAQ simulations, we used the following statistics. All are frequently used in the modeling community. Observational EPA AQS data were used to validate model results.

Correlation (r) between model values and observed values

$$r = \frac{\sum_{t=1}^{n}[(x_t - \bar{x})(y_t - \bar{y})]}{\sqrt{\sum_{t=1}^{n}(x_t - \bar{x})^2 * \sum_{t=1}^{n}(y_t - \bar{y})^2}} \qquad (7)$$

n = number of data points, x = observed values, y = model values, and values with an over bar indicate the mean.

Index of Agreement (IOA) between model values and observed values

$$IOA = 1 - \frac{\sum_{t=1}^{n} e_t^2}{\sum_{t=1}^{n}(|y_t - \bar{x}| + |x_t - \bar{x}|)^2} \qquad (8)$$

n = number of data points, $e_t = y_t - x_t$, x = observed values, y = model values, and values with an over bar indicate the mean.

Root Mean Square Error (RMSE)

$$RMSE = \sqrt{\frac{1}{n}\sum_{t=1}^{n} e_t^2} \qquad (9)$$

n = number of data points, $e_t = y_t - x_t$, x = observed values, y = model values

Mean Absolute Error (MAE)

$$MAE = \frac{1}{n}\sum_{t=1}^{n} |e_t| \qquad (10)$$

n = number of data points, $e_t = y_t - x_t$, x = observed values, y = model values

Mean Bias (MB)

$$MB = \frac{1}{n}\sum_{t=1}^{n} e_t \qquad (11)$$

n = number of data points, $e_t = y_t - x_t$, x = observed values, y = model values

.

Acknowledgments

References

Carfrae, J. A., Sheppard, L. J., Raven, J. A., Leith, I. D., Stein, W., Crossley, A., & Theobald, M. (2004). Early effects of atmospheric ammonia deposition on Calluna vulgaris (L.) hull growing on an ombrotrophic peat bog. *Water, Air, and Soil Pollution: Focus*, *4*(6), 229–239. https://doi.org/10.1007/s11267-004-3033-1

Cheng, B., & Wang-Li, L. (2019). Responses of secondary inorganic PM2.5 to precursor gases in an Ammonia Abundant area in North Carolina. *Aerosol and Air Quality Research*, *19*(5), 1126–1138. https://doi.org/10.4209/aaqr.2018.10.0384

Dammers, E., McLinden, C. A., Griffin, D., Shephard, M. W., Van Der Graaf, S., Lutsch, E., Schaap, M., Gainairu-Matz, Y., Fioletov, V., Van Damme, M., Whitburn, S., Clarisse, L., Cady-Pereira, K., Clerbaux, C., Francois Coheur, P., & Erisman, J. W. (2019). NH3 emissions from large point sources derived from CrIS and IASI satellite observations. *Atmospheric Chemistry and Physics*, *19*(19), 12261–12293. https://doi.org/10.5194/ACP-19-12261-2019

Dammers, E., Palm, M., Damme, M. Van, Vigouroux, C., Smale, D., Conway, S., Toon, G. C., Jones, N., Nussbaumer, E., Warneke, T., Petri, C., Clarisse, L., Clerbaux, C., Hermans, C., Lutsch, E., Strong, K., Hannigan, J. W., Nakajima, H., Morino, I., … Erisman, J. W. (2016). An evaluation of IASI-NH 3 with ground-based Fourier transform infrared spectroscopy measurements. *Atmos. Chem. Phys*, *16*, 10351–10368. https://doi.org/10.5194/acp-16-10351-2016

Dammers, E., Shephard, M. W., Palm, M., Cady-Pereira, K., Capps, S., Lutsch, E., Strong, K., Hannigan, J. W., Ortega, I., Toon, G. C., Stremme, W., Grutter, M., Jones, N., Smale, D., Siemons, J., Hrpcek, K., Tremblay, D., Schaap, M., Notholt, J., & Erisman, J. W. (2017).

Validation of the CrIS fast physical NH3 retrieval with ground-based FTIR. *Atmos. Meas. Tech.*, *10*(7), 2645–2667. https://doi.org/10.5194/amt-10-2645-2017

Ge, S., Wang, S., Xu, Q., & Ho, T. (2021). Characterization and sensitivity analysis on ozone pollution over the Beaumont-Port Arthur Area in Texas of USA through source apportionment technologies. *Atmospheric Research*, *247*, 105249. https://doi.org/10.1016/J.ATMOSRES.2020.105249

Hauglustaine, D. A., Balkanski, Y., & Schulz, M. (2014). A global model simulation of present and future nitrate aerosols and their direct radiative forcing of climate. *Atmospheric Chemistry and Physics*, *14*(20), 11031–11063. https://doi.org/10.5194/acp-14-11031-2014

Herron-Thorpe, F. L., Lamb, B. K., Mount, G. H., & Vaughan, J. K. (2010). Evaluation of a regional air quality forecast model for tropospheric NO2 columns using the OMI/Aura satellite tropospheric NO2 product. *Atmospheric Chemistry and Physics*, *10*(18), 8839–8854. https://doi.org/10.5194/ACP-10-8839-2010

Holland, H. D., & Turekian, K. K. (2014). *Treatise on Geochemistry* (Second). Elsevier. https://doi.org/https://doi.org/10.1016/B978-0-08-095975-7.00410-1

Howard, C. M. (2011). The European Nitrogen Assessment. *The European Nitrogen Assessment*, *January*. https://doi.org/10.1017/cbo9780511976988

Huang, M., Xu, J., Cai, S., Liu, X., Zhao, W., Hu, C., Gu, X., Fang, L., & Zhang, W. (2018). Characterization of brown carbon constituents of benzene secondary organic aerosol aged with ammonia. *Journal of Atmospheric Chemistry*, *75*(2), 205–218. https://doi.org/10.1007/s10874-017-9372-x

Kumar, A., Marcolli, C., Luo, B., & Peter, T. (2018). Enhanced ice nucleation efficiency of microcline immersed in dilute NH<sub>3</sub> and NH<sub>4</sub><sup>+</sup>-containing solutions. *Atmospheric Chemistry and Physics Discussions*, *January*, 1–32. https://doi.org/10.5194/acp-2018-46

Momeni, M., Choi, Y., Yeganeh, A. K., Pouyaei, A., Jung, J., Park, J., Shephard, M. W., Dammers, E., & Cady-Pereira, K. E. (2023). Constraining East Asia Ammonia Emissions Through Satellite Observations and Iterative Finite Difference Mass Balance (iFDMB) and Investigating its Impact on Inorganic Fine Particulate Matter. *Social Science Research Network*. https://doi.org/10.2139/SSRN.4395242

Paerl, H. W., Dennis, R. L., & Whitall, D. R. (2002). Atmospheric deposition of nitrogen: Implications for nutrient over-enrichment of coastal waters. *Estuaries*, *25*(4), 677–693. https://doi.org/10.1007/BF02804899

Paulot, F., Jacob, D. J., Johnson, M. T., Bell, T. G., Baker, A. R., Keene, W. C., Lima, I. D., Doney, S. C., & Stock, C. A. (2015). Global oceanic emission of ammonia: Constraints from seawater and atmospheric observations. *Global Biogeochemical Cycles*, *29*(8), 1165–1178. https://doi.org/10.1002/2015GB005106

Paulot, F., Jacob, D. J., Pinder, R. W., Bash, J. O., Travis, K., & Henze, D. K. (2014). Ammonia emissions in the United States, European Union, and China derived by high-resolution inversion of ammonium wet deposition data: Interpretation with a new agricultural emissions inventory (MASAGE_NH3). *J. Geophys. Res. Atmos*, *119*, 4343–4364. https://doi.org/10.1002/2013JD021130

Pinder, R. W., Bettez, N. D., Bonan, G. B., Greaver, T. L., Wieder, W. R., Schlesinger, W. H., & Davidson, E. A. (2013). Impacts of human alteration of the nitrogen cycle in the US on radiative forcing. *Biogeochemistry*, *114*(1–3), 25–40. https://doi.org/10.1007/s10533-012-9787-z

Pui, D. Y. H., Chen, S. C., & Zuo, Z. (2014). PM2.5 in China: Measurements, sources, visibility and health effects, and mitigation. *Particuology*, *13*(1), 1–26. https://doi.org/10.1016/j.partic.2013.11.001

Seinfeld, J. H., & Pandis, S. N. (2016). *Atmospheric chemistry and physics : from air pollution to climate change*. John Wiley & Sons, Inc. https://www.wiley.com/en-us/Atmospheric+Chemistry+and+Physics%3A+From+Air+Pollution+to+Climate+Change%2C+3rd+Edition-p-9781119221173

Van Damme, M., Erisman, J. W., Clarisse, L., Dammers, E., Whitburn, S., Clerbaux, C., Dolman, A. J., & Coheur, P.-F. (2015). Worldwide spatiotemporal atmospheric ammonia (NH₃) columns variability revealed by satellite. *Geophysical Research Letters*, *42*(20), 8660–8668. https://doi.org/10.1002/2015GL065496

Woo, J. H., Kim, Y., Kim, H. K., Choi, K. C., Eum, J. H., Lee, J. B., Lim, J. H., Kim, J., & Seong, M. (2020). Development of the CREATE Inventory in Support of Integrated Climate and Air Quality Modeling for Asia. *Sustainability 2020, Vol. 12, Page 7930*, *12*(19), 7930. https://doi.org/10.3390/SU12197930

Xu Zhenying, X., Liu, M., Song, Y., Wang, S., Xu, Z., Zhang, M., Zhang, L., Xu, T., Wang, T., Yan, C., Zhou, T., Sun, Y., Pan, Y., Hu, M., Zheng, M., & Zhu, T. (2019). High efficiency of livestock ammonia emission controls in alleviating particulate nitrate during a severe winter haze episode in northern China. *Article in Atmospheric Chemistry and Physics*, *19*, 5605–5613. https://doi.org/10.5194/acp-19-5605-2019

Yang, W., Ma, Q., Liu, Y., Ma, J., Chu, B., Wang, L., & He, H. (2018). Role of NH3 in the Heterogeneous Formation of Secondary Inorganic Aerosols on Mineral Oxides. *Journal of Physical Chemistry A*, *122*(30), 6311–6320. https://doi.org/10.1021/acs.jpca.8b05130

Zhang, X., Kondragunta, S., & Roy, D. P. (2014). Interannual variation in biomass burning and fire seasonality derived from geostationary satellite data across the contiguous United States from 1995 to 2011. *Journal of Geophysical Research: Biogeosciences*, *119*(6), 1147–1162. https://doi.org/10.1002/2013JG002518

Zhu, L., Henze, D. K., Bash, J. O., Cady-Pereira, K. E., Shephard, M. W., Luo, M., & Capps, S. L. (2015a). Sources and Impacts of Atmospheric NH 3 : Current Understanding and Frontiers for Modeling, Measurements, and Remote Sensing in North America. *Current Pollution Reports 2015 1:2*, *1*(2), 95–116. https://doi.org/10.1007/S40726-015-0010-4

Zhu, L., Henze, D. K., Bash, J. O., Cady-Pereira, K. E., Shephard, M. W., Luo, M., & Capps, S. L. (2015b). Sources and Impacts of Atmospheric NH3: Current Understanding and Frontiers for Modeling, Measurements, and Remote Sensing in North America. *Current Pollution Reports*, *1*(2), 95–116. https://doi.org/10.1007/s40726-015-0010-4

Zhu, L., Henze, D. K., Cady-Pereira, K. E., Shephard, M. W., Luo, M., Pinder, R. W., Bash, J. O., & Jeong, G. R. (2013). Constraining U.S. ammonia emissions using TES remote sensing observations and the GEOS-Chem adjoint model. *Journal of Geophysical Research: Atmospheres*, *118*(8), 3355–3368. https://doi.org/10.1002/JGRD.50166